CAPITAL UNIVERSITY OF SCIENCE AND
TECHNOLOGY, ISLAMABAD

Genetic Algorithm based Multi-focus Image Fusion using Local Features

by

Muhammad Ubaid Ur Rehman

A thesis submitted in partial fulfillment for the
degree of Master of Science

in the

Faculty of Computing
Department of Computer Science

2020

This dissertation is dedicated to my parents, brothers, teachers, colleagues, friends and to all those who have lost their precious lives because of novel severe acute respiratory syndrome pandemic.

CERTIFICATE OF APPROVAL

Genetic Algorithm based Multi-focus Image Fusion using Local Features

by

Muhammad Ubaid Ur Rehman

(MCS173003)

THESIS EXAMINING COMMITTEE

S. No.	Examiner	Name	Organization
(a)	External Examiner	Dr. Waseem Shahzad	NUCES, Islamabad
(b)	Internal Examiner	Dr. M. Masroor Ahmed	CUST, Islamabad
(c)	Supervisor	Dr. Abdul Basit Siddiqui	CUST, Islamabad

Dr. Abdul Basit Siddiqui
Thesis Supervisor
December, 2020

Dr. Nayyer Masood
Head
Dept. of Computer Science
December, 2020

Dr. Muhammad Abdul Qadir
Dean
Faculty of Computing
December, 2020

Author's Declaration

I, **Muhammad Ubaid Ur Rehman** hereby state that my MS thesis titled "**Genetic Algorithm based Multi-focus Image Fusion using Local Features**" is my own work and has not been submitted previously by me for taking any degree from Capital University of Science and Technology, Islamabad or anywhere else in the country/abroad.

At any time if my statement is found to be incorrect even after my graduation, the University has the right to withdraw my MS Degree.

(Muhammad Ubaid Ur Rehman)
Registration No: MCS173003

Plagiarism Undertaking

I solemnly declare that research work presented in this thesis titled "**Genetic Algorithm based Multi-focus Image Fusion using Local Features**" is solely my research work with no significant contribution from any other person. Small contribution/help wherever taken has been duly acknowledged and that complete thesis has been written by me.

I understand the zero tolerance policy of the HEC and Capital University of Science and Technology towards plagiarism. Therefore, I as an author of the above titled thesis declare that no portion of my thesis has been plagiarized and any material used as reference is properly referred/cited.

I undertake that if I am found guilty of any formal plagiarism in the above titled thesis even after award of MS Degree, the University reserves the right to withdraw/revoke my MS degree and that HEC and the University have the right to publish my name on the HEC/University website on which names of students are placed who submitted plagiarized work.

(Muhammad Ubaid Ur Rehman)
Registration No: MCS173003

Acknowledgements

First of all, I am thankful to Almighty ALLAH, the most gracious, the most merciful, for making me able to accomplish this achievement of my life.

Secondly, I would like to express my sincere gratitude to my thesis supervisor Dr. Abdul Basit Siddiqui, who introduced me to the emerging domain of image fusion in digital image processing. Without his endless support, valuable suggestions and positive feedback, it was not possible to complete this dissertation.

I express my best wishes to colleagues and friends for their support and motivation throughout this study.

In the end, I present a bundle of thanks to my parents and other family members, for their prayers and countless support during ups and downs, hot and cold which I experienced during my work so that I could reach up to this goal.

(Muhammad Ubaid Ur Rehman)
Registration No: MCS173003

Abstract

Recent developments in the domain of information technology have made it possible to extract a knowledge of ocean from input images. The knowledge extraction can be performed using a number of operations such as image segmentation. The major objective of image segmentation is to segment focused and non-focused regions from an input image. The field depth of optical lenses is limited. A camera focuses only on those objects which lie in its field depth, rest of the objects are appeared as non-focused or blurry. For image processing, it is a general requirement that an input image must be all in focus image. In almost each domain such as medical imaging, weapon and aircraft detection, digital photography and agriculture imaging, it is required to have an all in focused input image. Image fusion is a process which combines two or more input images to create an all in focused complimentary fused image. Image fusion is considered as a challenging task due to irregular boundaries of focused and non-focused regions. In literature, multiple studies have addressed this issue, however they have reported promising results in creating a fully focused fused image. Moreover, they have considered different features to identify focused and non-focused regions from an input image. For better estimation of focused and non-focused regions, an ensemble of multiple features such as shape and texture based features can be employed. Furthermore, it is required to obtain optimal weights which are to be assigned to each feature for creating a fused image. The focus of this study is to perform a multi-focus image fusion using an ensemble of multiple local features by weight optimization using a genetic algorithm. To perform this experimentation, nine multi-focus image datasets are collected where each dataset indicates an image pair of multi-focused images. The reason of this selection is two-fold, as they are publicly available and it contain different types of multi-focus images. For reconstruction of a fully focused fused image, an ensemble of different shape and texture based features such as Sobel Operator, Laplacian Operator and Local Binary Pattern is employed along with optimal weights obtained using a Genetic Algorithm. The experimental results have indicated improvement over previous fusion methods.

Contents

List of Figures

Abbreviations

AG	Gradient Based Fusion Evaluation
CAB	Content Adaptive Blur
CBF	Cross Bilateral Filter
CSR	Convolutional Sparse Representation
DCTV	Image Fusion for Visual Sensor Networks in DCT Domain
DCHWT	Discrete Cosine Harmonic Wavelet Transform
DCTLP	Discrete Cosine Transform using Laplacian Pyramid
GIF	Guided Image Fusion
ICA	Independent Component Analysis
IFM	Image Matting for Fusion
IFGD	Image Fusion in Gradient Domain
MWGF	Multi-scale Weighted Gradient Fusion
MSTSR	Multi-scale Transform Sparse Representation
NMI	Normalized Mutual Information Based Fusion Evaluation
PCA	Principal Component Analysis
PCNN	Pulse Coupled Neural Network
SRCF	Dictionary-Based Sparse Representation
WSSM	Wavelet Based Statistical Sharpness
YC	Structural Similarity Based Fusion Evaluation

Symbols

$I_1(x, y)$	First Input Image
$I_2(x, y)$	Second Input Image
$I_F(x, y)$	Fused Image
ω_{LBP}	Local Binary Pattern Operator
ω_{LO}	Laplacian Operator
ω_{SO}	Sobel Operator
$\alpha_{\omega_{LBP_1}}$	Local Binary Pattern Image using Input Image One
$\alpha_{\omega_{LO_1}}$	Laplacian Operator Image using Input Image One
$\alpha_{\omega_{SO_1}}$	Sobel Operator Image using Input Image One
$\alpha_{\omega_{LBP_2}}$	Local Binary Pattern Image using Input Image Two
$\alpha_{\omega_{LO_2}}$	Laplacian Operator Image using Input Image Two
$\alpha_{\omega_{SO_2}}$	Sobel Operator Image using Input Image Two
$\alpha'_1(x, y)$	Combined Activity Image using Input Image One
$\alpha'_2(x, y)$	Combined Activity Image using Input Image Two

Chapter 1

Introduction

1.1 Motivation

With the advancements in the domain of information technology, there exists a deep knowledge of ocean in images from which a user intends to retrieve a relevant and specific information. By using certain number of applications, a user can extract multiple types of knowledge from images such as a creation of augmented reality-based three-dimensional simulation of skull to perform an accurate on-line surgical treatment of oral and maxillofacial infections [1]. Similarly, radiologists can use multiple imaging modalities including x-ray, positron emission tomography, computed tomography and magnetic resonance imaging for detection of acute diseases [2].

A user is required to perform a set of operations at the time of knowledge extraction which includes image segmentation and registration etc. The main goal of segmentation is to segment focused and non-focused regions in a particular image for image restoration [3]. For image processing, an input source image should be an all in focused image. Now a day, each user can capture different aspects of human life using imaging devices. The focus range of imaging devices is limited; therefore, these devices focus only on those objects which lie in its range, rest of the objects in an image tends to appear as blurry or non-focused [4].

An image is a kind of an artifact which draws a visual interpretation of a particular object in a form of two-dimensional photograph or a simple picture. Images can exist in multi-dimensions; however, the most common types of multidimensional images are two-dimensional [5] and three-dimensional images [6]. The examples of two-dimensional images are photographs, screen displays etc. Similarly, hologram or a statue is an example of three-dimensional images. The images are usually captured through photo sensing devices such as cameras, microscopes, telescopes, magnetic resonance imaging and photon emission photography etc.

An image in a real world can be defined as a function of two real time variables such as $I(x, y)$ having a manipulation of multiple color pixels in x, y coordinate system. Advancement in the technology, have made it possible to process multi-dimensional images from simple digital images to advanced digital images such as electromagnetic radiations or waves to convey a particular information. Generally, an image is a combination of multiple sub-images which can be titled as regions of interest, or simply regions. In other words, we can say, an image contains a collection of objects with respect to a particular region. However, modern image processing has made it possible to select any particular region in an image to classify a particular object. The reason for this processing is two-fold; as one wants to remove the motion blur from a particular region of interest, however, other can use this to enhance a particular image in terms of its intensity.

It is a general requirement of image processing, that an image should be available in a finite size array of bits. Therefore, at the time of image processing each image is modeled over x, y coordinate system where each pixel of an image is quantized using a particular bit sequence [7]. The image processing can be further classified into two categories such as computer graphics and computer vision. In computer graphics, a user manually creates a particular image using multiple image objects such as environment, lightings etc. without capturing them from a natural environment. The most common examples of computer graphics are animated movies [8]. On the other hand computer vision is a high-level image processing, where a system intends to retrieve a signature of a particular information from sequence of images such as magnetic resonance imaging etc. [9]. Now a day, image processing

has become the focus of multiple scientists, because of its exponentially growing scope in scientific visualization. Currently, the scientists are solving multiple problems of science using a powerful tool of image processing.

1.2 Classification of Digital Images

Digital images can be further classified into multiple types such as Binary Image, Grayscale Image, Color Image and Multispectral Images etc. as mentioned in 1.1 below.

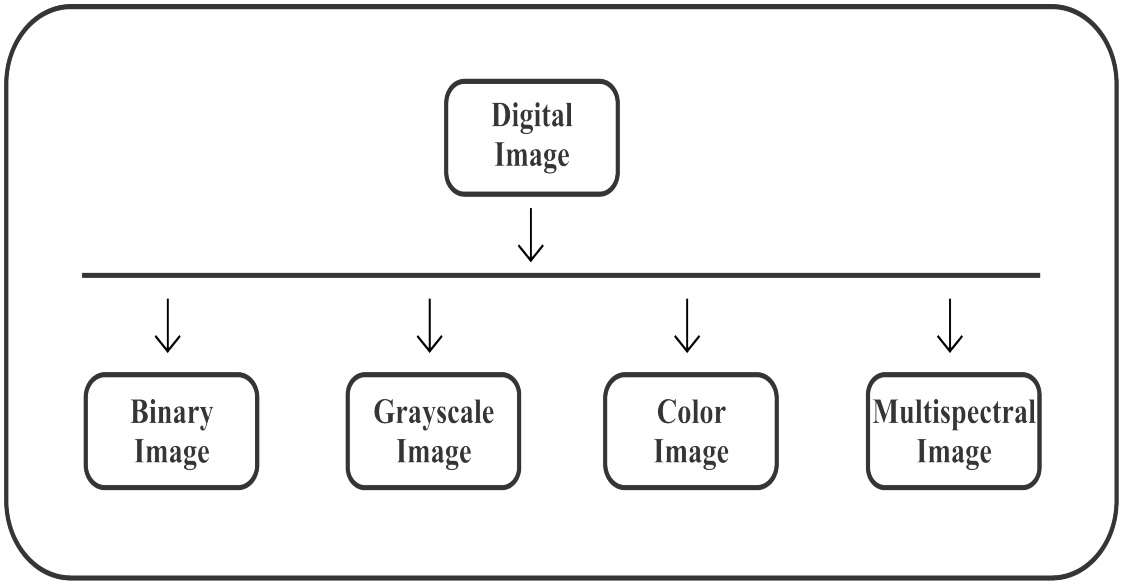

FIGURE 1.1: Classification of Digital Images.

1.2.1 Binary Images

The binary images are known as a simple type of images, as they only require two types of pixel values such as Black or White. Usually black color is marked as 0, whereas 1 represents a white color. In general, Black and white images are also referred as one-bit images, as they only require one bit to indicate a particular pixel value. This kind of images are often used in the applications where information is available in shape outline. The most common example of such applications is character recognition [10].

1.2.2 Grayscale Images

The grayscale images are represented as one-color image, as it only contains the grey level information, however, it does not contain any color values. In grayscale images, each image pixel is represented using a specific sequence of bits which determine its gray levels. Typically, eight data bits are used to represent a pixel which allows the creation of 256 gray levels in a particular pixel. The grayscale images are widely used in almost all type of image processing applications such as medical, astronomy. etc. [11].

1.2.3 Color Images

The color images are referred as three channel images, where each channel indicates a particular color. The actual information is a gray level information which is stored in each channel respectively. Generally, the color images are modeled using three colors such as Red, Green, Blue (RGB) colors. In color images, each color channel requires 8-bit pixel value. The resultant image would be of 24-bit color values [12]. Figure 1.2, below presents a visualization of an image in RGB color space.

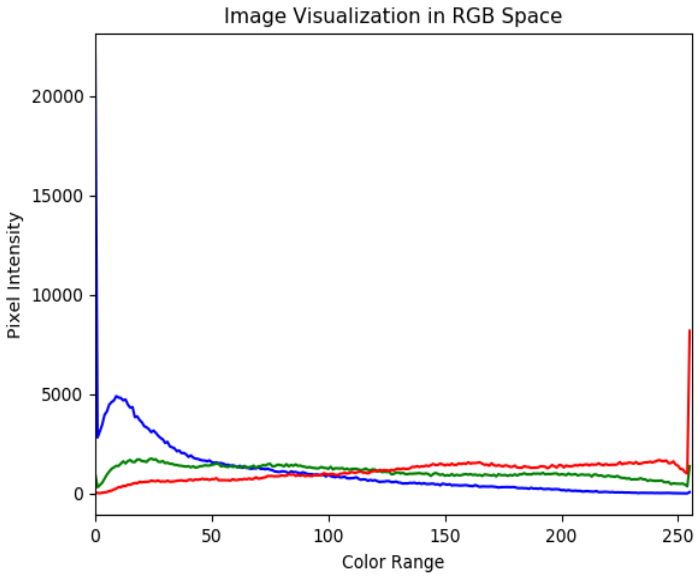

FIGURE 1.2: Visualization of an Image in RGB Color Space.

1.2.4 Multispectral Images

Multispectral images hold a kind of information which is beyond the human perception. This kind of images contain ultraviolet, X-Ray, infrared and radar data. The information in the multispectral images is not directly visible to a human, however, a particular information can be visualized by the mapping of multiple color bands [13].

1.3 Types of Blurs

Blur in an image usually occurs, when one experiences a camera shake during photography. Blur is a kind of an undesirable artifact which reduces the sharpness and contrast of an image. There exists a difference between blur and out of focus. Non-focused regions in an image only appears when a particular region lies away from the focus axis of a camera device. Figure 1.3 below, indicates a strong relationship between blur and visibility. As it is visible in chart below, an increase in blur reduces sharpness.

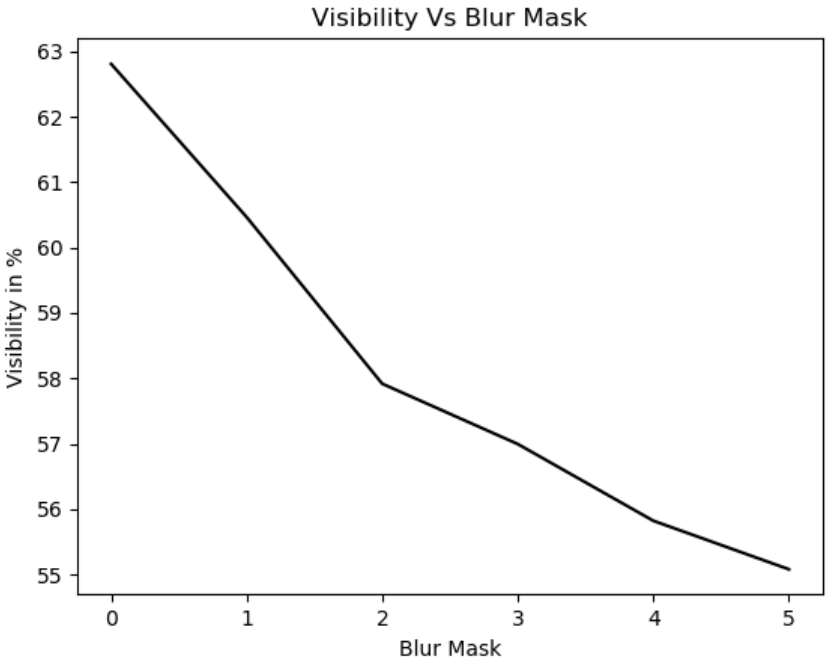

FIGURE 1.3: Effect of Blur on Image Visibility.

However, in computer vision a blur is applied to remove outliers or noise from a particular image. The blur can be further classified into two types such as artistic blur and motion blur which can be visualized in figure 1.4 below.

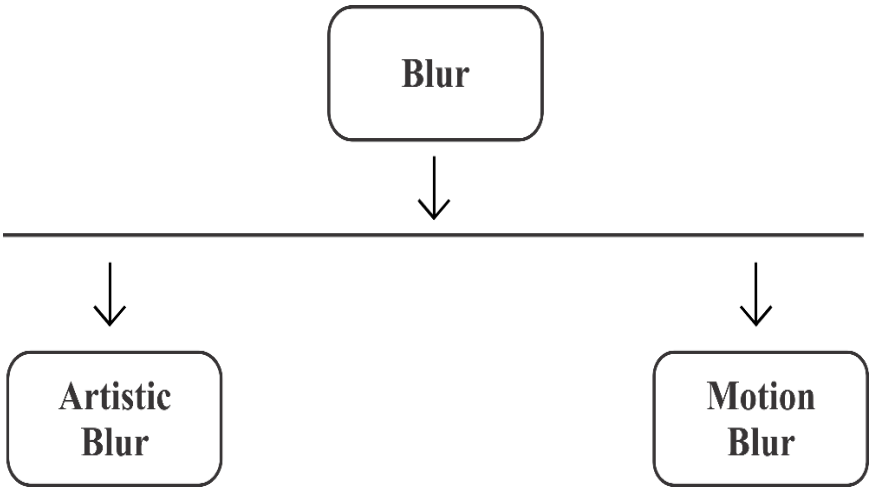

FIGURE 1.4: Types of Blur in Images.

1.3.1 Artistic Blur

Artistic blur is a kind of intentional blur, which is introduced by a camera device to make a focus on a particular object. Rest of the objects of a particular scene will tend to be appeared as out of focused or blurry. In other words, it is occurred due to limited field depth of a camera.

1.3.2 Motion Blur

Motion blur in an image only appears, when a particular object of a scene is in motion. The motion blur is usually occurred when shutter speed is slow and one experiences a motion in a scene. For instance, if shutter speed is $\frac{1}{30}$th of a second and a particular object is moving in a scene, then that object will appear as blurry in a scene. When a camera device captures a particular scene, it does not represent a single instance of time. Because of technological aspects, it may capture a scene over different time periods. At the time of objects motion in a particular frame, one must include all of its positions.

1.4 Image Fusion

Field depth also known as a focus range of optical lenses. Field depth is used to estimate distance between nearest and farthest artifacts in an image. Due to limited field depth of camera lenses, camera focuses only on the areas which lie in its focus plane [14]. As a result, some regions in an image might be out of focus or blurred. A renowned methodology to address this issue is multi-focus image fusion. Data fusion is a process, which uses information and data which is being generated from multiple sources to obtain refined information for decision making. Generally, image fusion is a process, that combines spatial detail from two or more input images to create a new contemporary image by using a specific methodology [15]. During the process of image fusion, image $I_1(x, y)$ and $I_2(x, y)$ are fused into a new contemporary image $I_F(x, y)$, figure 1.5 below presents the visual interpretation of this phenomena.

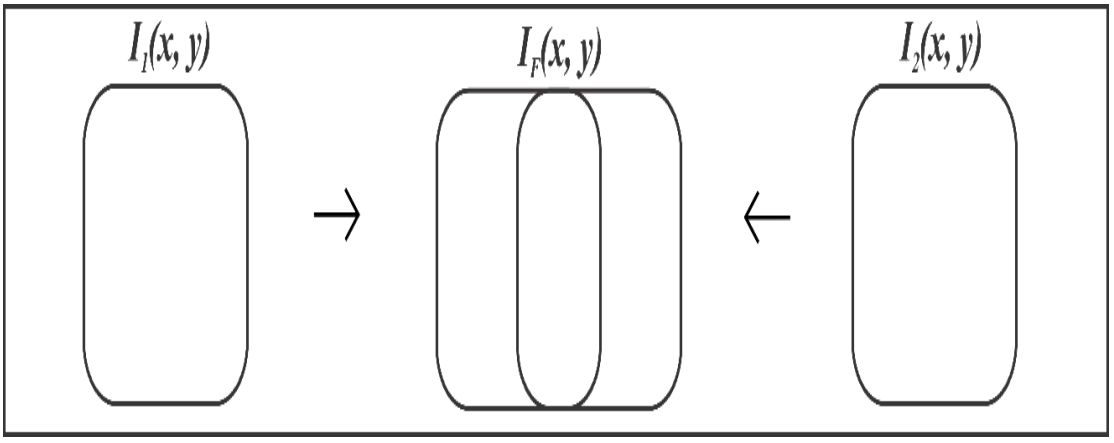

FIGURE 1.5: Principle of Image Fusion.

Similarly, Multi-focus image fusion is a process of generating a composite image which enhances the field depth of an image. Enhanced field depth creates an image with efficient focus range using a set of multi-focus images. A composite image which is also known as a fused image, will be more appropriate for multiple image processing applications as well as for human perception. Image fusion can be of two types such as Spatial Domain Image Fusion and Transform Domain Image Fusion [16]. Figure 1.6 presents a visual interpretation of this classification.

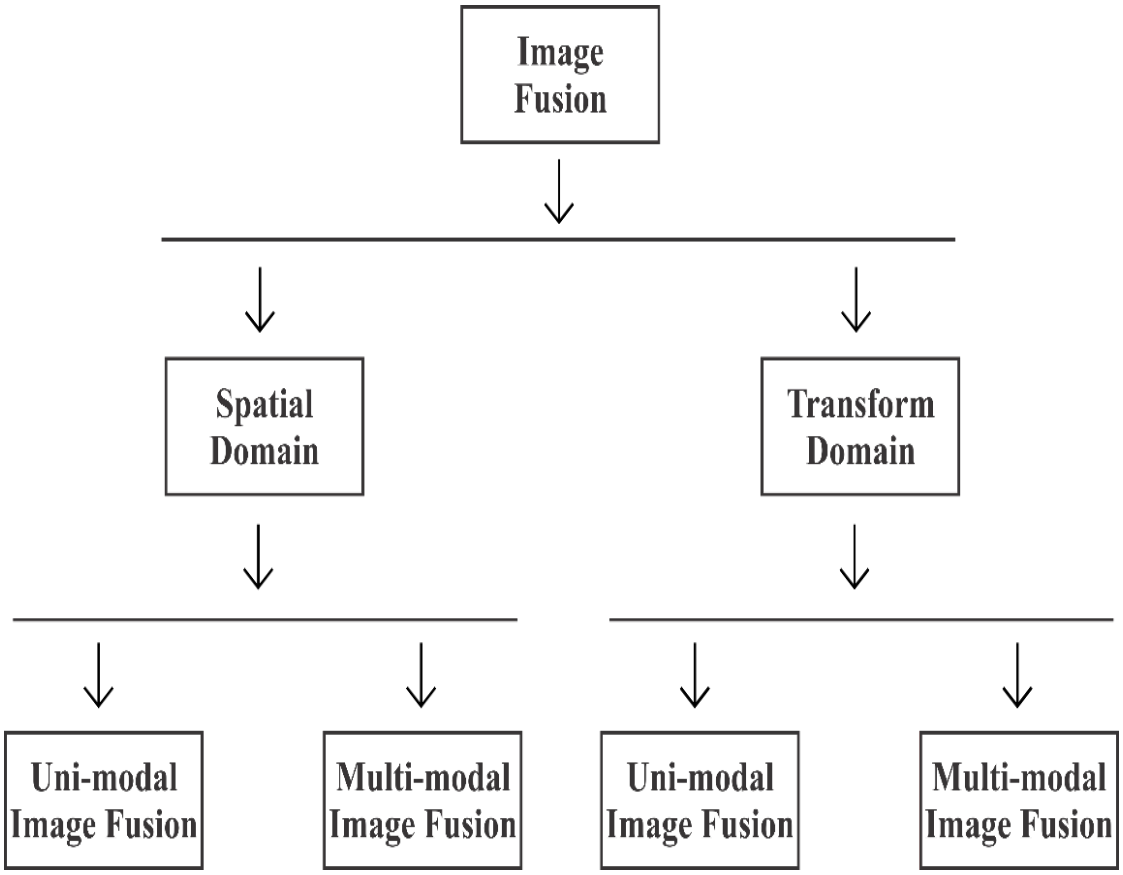

FIGURE 1.6: Domains of Image Fusion.

1.4.1 Spatial Domain Image Fusion

In spatial domain image fusion, the sharpness and different focus measures can be calculated directly from image pixels or image blocks of size $n \times n$ [17]. However, focus estimation can be done in multiple ways. Therefore, fusion methods of this domain can be classified into three classes such as image block based, image pixel-based and region-based methods. These methods can be implemented easily with low computational cost. The fused image contains more focused regions than input image.

1.4.2 Transform Domain Image Fusion

In the transform domain image fusion, input image is first converted into transform domain and then image coefficients are fused to obtain a focused image [18]. We

can classify its fusion methods into multiple classes such as sparse representation-based image fusion and wavelet transform based image fusion. The sparse representation indicates the processing of natural signals which is very closed to human visual system. Lets consider an input signal $I_S \in R^{n \times m}$ and a dictionary $D \in R^{n \times m}$ The basic goal of sparse representation is to estimate a sparse vector $v \in R^{n \times m}$ with a lesser number of non-zero entries such that $D \approx I_S \times v$ [19]. Similarly, wavelet transform calculates the correlation between a signal which is to be analyzed and wavelet function at different scales [20]. However, both of these fusion methodologies can be implemented into two domains such as unimodal image fusion or multimodal image fusion.

1.4.3 Unimodal Image Fusion

Figure 1.7 below presents an analysis of unimodal image fusion system. The image sensor in this approach can be a digital camera. The mentioned image sensor captures a sequence of real-world photos. Later, the captured sequence is then fused into a single fused image which can be processed by a scientist or by a computer program for multiple purposes. For example, in unidentified aircraft detection, where one wants to detect an enemy aircraft for security purposes. However, this system has a certain number of limitations regarding capability of an image sensor.

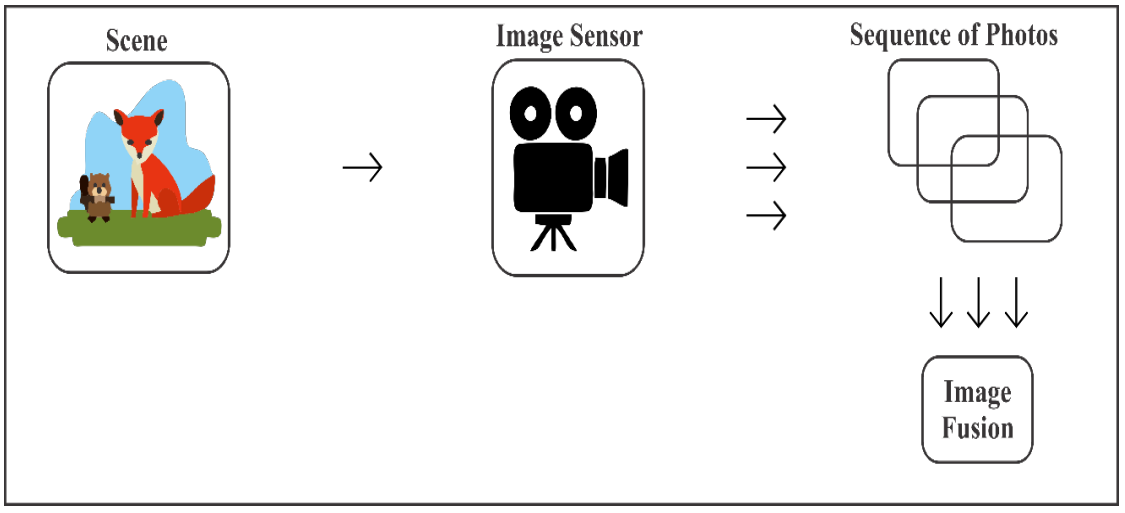

FIGURE 1.7: Anatomy of Unimodal Image Fusion.

1.4.4 Multimodal Image Fusion

In this system, one combines a sequence of images captured using multiple image sensors into a single composite fused image. In this scenario, one image sensor can be an infrared camera and other sensor can be a digital camera. This methodology has addressed the limitations of unimodal image fusion system. As digital camera is only suitable for bright light photography, however, infrared camera can perform better in poor lightening conditions as well. For this reason, radiologists prefer usage of multi-modal images to obtain more specific details for efficient detection of medical problems such as glioblastoma, ductal carcinoma. This anatomy is illustrated in figure 1.8.

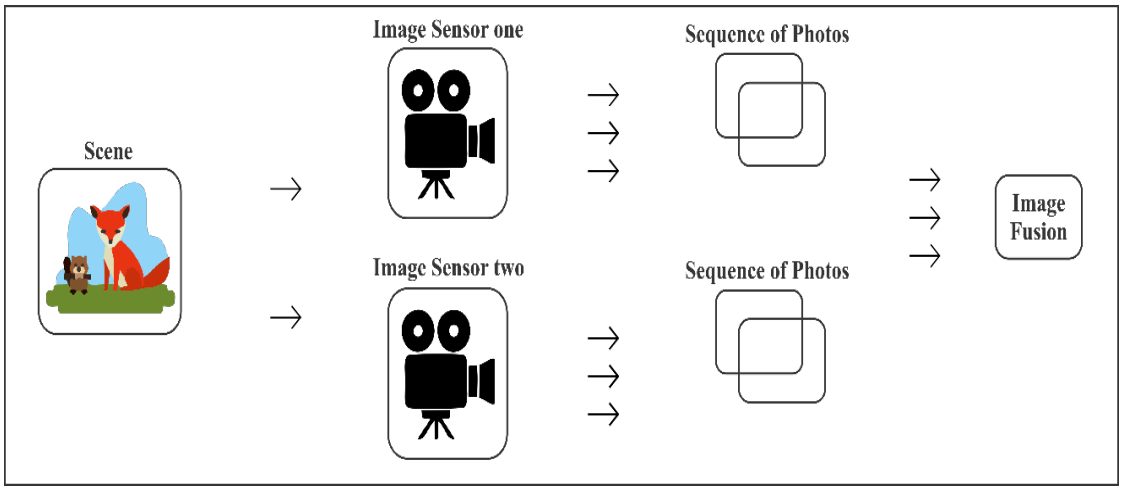

FIGURE 1.8: Investigation of Multi-Modal Image Fusion.

1.5 Applications of Image Fusion

There are multiple applications of image fusion which are enlisted below:

1.5.1 Weapon and Aircraft Detection

Image fusion is considered as an important research topic in weapon and aircraft detection [21]. In this type of image fusion, one combines a set of images captured using multiple image modalities such as Infrared image and a visual image.

The infrared image contains vital and specific target information which cannot be available in visual images. Similarly, visual images can have the information of all scattered objects from a particular scene. Therefore, visual images are only used for information extraction. Figure 1.9 below, presents an illustration of target detection using image fusion.

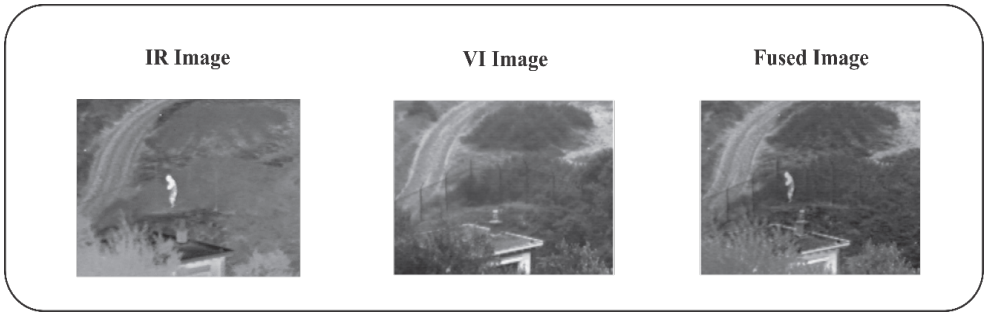

FIGURE 1.9: Target Detection using Image Fusion.

1.5.2 Medical Imaging

The advancements in the medical domain have made it possible to cure multiple infectious diseases with the help of image fusion [22]. In this case, a medical practitioner combines a set of images of a patient to obtain more accurate information. A medical fused image can be obtained by merging multiple input image from a unimodal imaging system or by combining the images of multiple modal such as Magnetic Resonance Imaging (MRI), Computed Tomography (CT), Positron Emission Tomography (PET), Single Photon Emission Computed Tomography (SPECT). Figure 1.10, below presents a view of multi modal image fusion in medical domain.

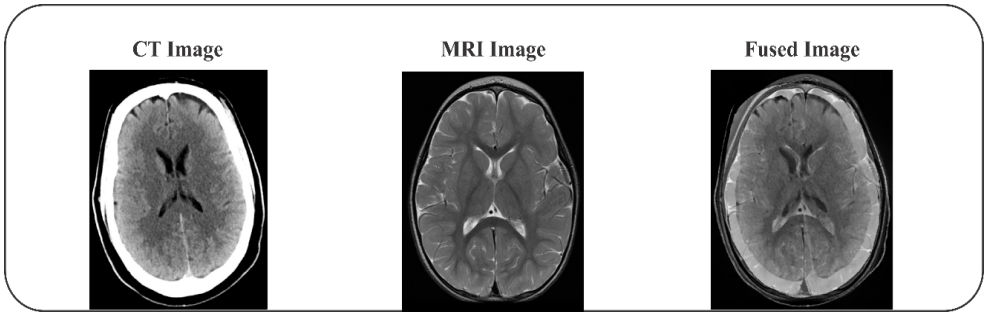

FIGURE 1.10: Multi-Modal Image Fusion in Medical.

1.5.3 Agriculture Imaging

Recent development in the agricultural domain has made it manageable to detect multiple diseases in the plants, crops and fruits. In this scenario, the agriculture scientist combines multiple images of plants captured using fluorescence technology to obtain more accurate detail about a particular feature, disease in a plant. Similarly, the approach of image fusion can be used to detect animal feces over a particular food item such as fruits, vegetable, meat which cannot be seen by naked eye [23].

1.5.4 Digital Photography

Image fusion can be implemented in modern digital photography to enhance the visual quality of an image. In this type of photography, a photographer combines multiple input images with different exposure levels into one single combined image. The resultant image will be more appealing in terms of visual quality than any other image. Figure 1.11, draws an illustration of multi exposure image fusion [24].

FIGURE 1.11: Glimpse of Multi-Exposure Image Fusion.

1.6 Problem Statement

Image fusion is a challenging task due to irregular boundaries of focused and non-focused regions. In literature, different features have been employed to characterize

focused parts in an image. For better results, an ensemble of different shape and texture based features can be used for better characterization of focused and non focused regions. Furthermore, it is required tofindoptimalweights of different features to define their individual contribution in a fused image.

1.7 Research Questions

Q1: How shape and texture in focused and non-focused regions are affected due to blurriness in input images?

Q2: What is the effect of increasing or decreasing neighborhood size around a pixel on the shape and texture of blurred and non-blurred regions in input images?

Q3: How maximal information can be obtained in fused image from input images using shape and texture-based features?

1.8 Thesis Layout

The rest of the thesis can be organized as follow:

1.8.1 Chapter 2

Chapter 2 of this study presents a critical review of previously proposed state of the art approaches for multi-focus image fusion methodologies in spatial and frequency domains.

1.8.2 Chapter 3

Chapter 3 of this study contains research methodology, which draws an illustration of adopted fusion method to fuse multiple images in this dissertation; however, it also contains most important local feature algorithms related to this study.

1.8.3 Chapter 4

This chapter discusses about objective evaluation of fused images and depicts evaluation results which are computed using a certain number of traditional quality measures.

1.8.4 Chapter 5

This chapter presents conclusion of this study and draws a layout of future work.

Chapter 2

Literature Review

2.1 Spatial Domain Image Fusion

The study in [25] suggested a fusion methodology (illustrated in figure 2.1) to fuse source images into one single image with higher visual interpretation. In this paper, it is proposed to fuse input source images by weighted average, which can be computed by estimating weights obtained from the image detail extracted from the source images using a cross bilateral filter. The proposed approach was evaluated visually and quantitatively over number of multi-focus source images.

Another study [26] proposed a novel method for the multi-focus image fusion. In this study, authors have calculated energy of Laplacian to decide portions of input source images as focused or non-focused, however, majority filter spreads the focused pixels to their corresponding neighborhood pixels. To reduce the block effect, authors have applied an edge-preserving guided image filter. Later, they have evaluated their approach visually and quantitatively using certain number of quality measures.

Similarly, image fusion and registration has a significant impact in the civil and military setups, for example, it can be helpful in recognizing a target at ground/air level and in medical images. In this work [27], the approaches of wavelets and principal component analysis were implemented to preserve the spatial details of

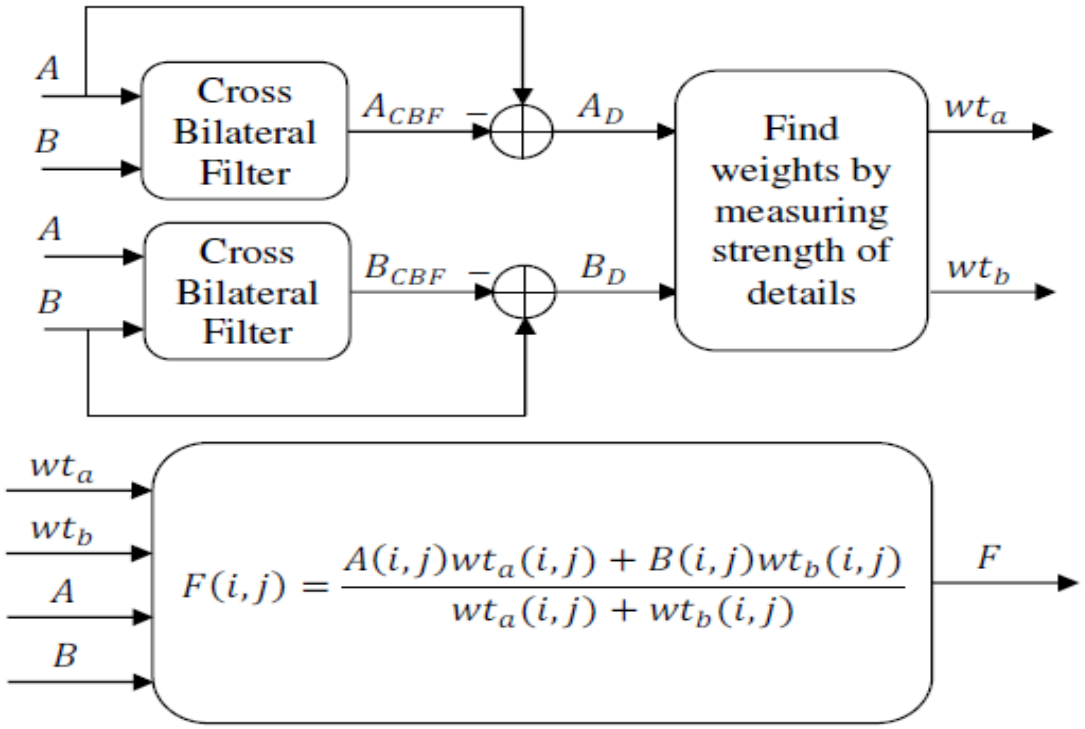

FIGURE 2.1: Fusion Methodology Proposed by Kumar et al [25]

multi-sensorial input source images into one single fused image. However, the proposed fusion approach was examined over number of referenced and non-referenced based images.

Pulse Coupled Neural Network (PCNN) [28] is proven to be an effective algorithm for image processing and fusion. Earlier studies have proposed PCNN based fusion algorithms which take input of one pixel which is not enough, as PCNN is inspired from the human neural system and humans are sensitive to features such as edges, texture and gradient etc. In this study, authors have considered orientation information as a one novel feature for image fusion. Later, they have evaluated their proposed procedure using visual and statistical evaluation measures.

Another study [29] has proposed a novel methodology to address the issue of multi-focus image fusion in spatial domain. In this study, authors have trained a dictionary using the local patches of input source images. Using the sparse representation of relevant sharpness measures, they obtained a decision map of focused and non-focused pixels. Later, the decision map was refined to generate

a composite all in focus image. This methodology was evaluated using certain number of visual and qualitative evaluation measures.

In another study [30], authors have suggested a novel methodology to generate a composite all in focused image using the gradient-based feature. In this study, they have used a weighted gradient to detect the focused and non-focused pixels of input source images. Using this classification, they create a rule base to fuse an image. Later, they evaluated their approach using certain quality metrics.

Hsieh et al [31] proposed a scheme to address the issue of multi-focus image fusion using color saturation. In their scheme, authors segment focused and non-focused regions of multi-focus images using star-light mask. On the basis of this segmentation, they generated an initial decision map which determines the number of activities in a particular image. Using these activity maps, they compared each pixel of an image, the one with high pixel intensity is selected for creation of a fused image.

Liu et al [32] has proposed a novel methodology to address the issue of multi-focus image fusion. In their approach, using a sliding window authors have calculated dense SIFT descriptors to obtain activity levels from multiple source image patches. On the basis of obtained descriptor, they created an initial decision map which contain multiple activities of an image, which is refined later for fusion.

Yin et al [33] proposed a new methodology for multi-focus image fusion. There methodology include a dictionary, which is created from sub-dictionaries. The sub-dictionaries are learned from multiple source images via sliding window using K-SVD algorithm. Authors have calculate sparse representation using batch-OMP algorithm. By combining trained dictionary and sparse representation, they created final rules for image fusion.

Zhang et al [34] suggested a novel approach for multi-focus image fusion using saliency analysis. Authors detected focused regions from multiple source images using GBVS algorithm. Later, they used watershed and morphological methods

to get a refined saliency map for fusion. Focused regions of source images are fused directly, however, remaining regions are fused using shearlet transform methods.

Zhao et al [4] has addressed the issue of multi-focus image fusion by suggesting a novel algorithm. In their approach, they have performed image fusion using nearest distance algorithm. The performance of this technique is highly dependent upon block size, as it is a block-based approach. To create a decision map for image fusion, authors subtracted coefficients of original image from its neighbor image.

The study of Tang et al [35] solved problem of multi-focus image fusion by using a Convolutional Neural Network (CNN). Authors have used CNN for the classification of pixels of source images as focused, defocused and uncertain. They generated an initial decision map by comparing intensities of input pixels. Later, they refined a decision map for image fusion by removing non-focused pixels.

Another study such as Farid et al [18] proposed a novel algorithm to neutralize the problem of multi-focus image fusion. Authors detected focused regions using Content Adaptive Blur algorithm. The said algorithm introduces a non-uniform blur in source images by determining image quality. They generated a decision map using difference between original image and blurred image. Later, this map is refined using morphological methods for image fusion.

Chantara et al [36] proposed a method for extension of field depth in source images. In their study, they used a spatial frequency and sum of Laplacian for estimation of image coefficients from source images. Using extracted coefficients, they decided focused regions from images which are later combined using image fusion.

Wang et al [37] discussed multi-focus image fusion by suggesting their novel approach. Authors performed image fusion using Laplacian operator and region optimization. They generated an initial decision map using Laplacian operator, as Laplacian efficiently detects focused and non-focused areas from source images. Later, they refined their decision map by using region optimization.

Li et al [38] addressed the issue of multi-focus image fusion using dynamic images of a particular scene. First, they extracted focus information of a relevant object

from a particular image by applying a morphological filter which created an initial decision map of active and non-active regions. Later, this map is further refined using image matting to get more accurate information about focused and non-focused regions. Authors claims that there approach has performed slightly better than other traditional approaches.

Paul et al [39] conducted a vigorous study on multi-exposure and multi-focus image fusion in gradient domain. In their study, authors have developed a gradient-based image fusion algorithm which treats image luminance and chrominance separately. First, it blends the gradients of luminance components of input images using the maximum gradient at each pixel location and later, it extracts the image chrominance using Haar wavelet-based image processing technique. According to study authors, their approach has produced some identical and better results than traditional multi-exposure and multi-focus image fusion algorithms.

Similarly, Zhou et al [30] suggested a novel multi-scale weighted gradient based fusion method to create a composite image from multi-focus input images. The anisotropic blur and mis-registration of image pixels usually occurs, while the photo sensing device is in motion, these types of factors severely degrade the quality of an image. The proposed method estimates the sharpness of active areas using edges and corners. This algorithm is based on image saliency and is being introduced to estimate the gradient weights. To effectively address the raised issues, authors have considered two-scales, i.e. small and large. The large scale is being used to detect the anisotropic blur and mis-registration however, the gradient weights can be obtained using small scale. As per the authors claim, there study has outperformed traditional fusion methods.

2.2 Transform Domain Image Fusion

The study of Liu et al [40] proposed a procedure for multi-focus image fusion in transform domain with a higher complementary information of source images in a fused image. In their approach, authors suggested usage of convolutional sparse

representation for image fusion. However, convolutional sparse representation-based image fusion is the advanced form of sparse representation-based image fusion. To validate effectiveness of the proposed approach, authors have evaluated their approach visually and quantitatively.

In another study Mitianoudis et al [41] proposed the notion (presented in figure 2.2) of preserving the active areas of multi-focus input images in a composite image. In this study, authors have implemented the approaches of independent component analysis (ICA) and topographical independent component analysis using novel fusion rules to create a particular composite image in transform domain. According to study authors, there approach have performed slightly better than traditional wavelet approaches.

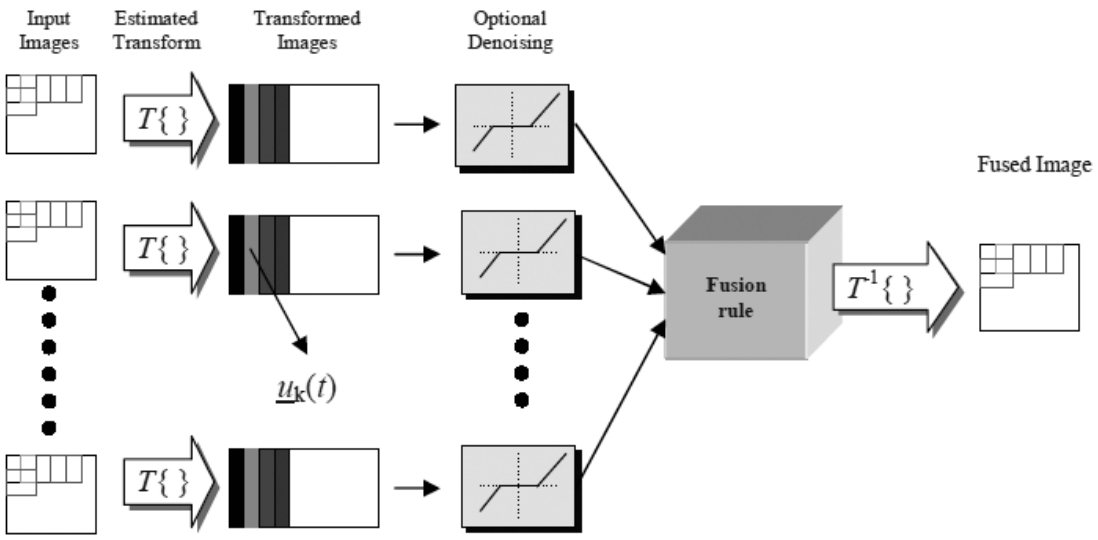

FIGURE 2.2: Fusion Methodology Proposed by Mitianoudis et al [41].

Similarly, Kumar et al [42] suggested a discrete cosine harmonic wavelet transform based image fusion method. The energy closeness and multi-resolution properties of wavelet have made the image fusion successful. Using the wavelet filter, one can effectively preserve the image features such as edges, texture etc. in a composite image without introducing any artifacts and enhancements. The wavelet can be visualized as a convolution of wavelet components of input images under consideration; however, it is computationally expensive. The lifting based fusion

approach has reduced number of computations at the cost of quality degradation and fusion process. To efficiently, preserve the image quality and fusion process, authors have introduced an aforementioned methodology, performance wise it is equivalent to convolutional and lifting based approaches.

Another study of Naidu et al [43] addressed the issue of multi-focus and multi-modal image by suggesting their approach in transform domain image fusion. In this study, authors have presented a novel approach which uses a discrete cosine transform based on Laplacian pyramid. However, image quality in the fused image can be enhanced using a higher number of pyramids.

Similarly, Bagher et al [44] proposed a novel methodology to solve problem of multi-focus image fusion in transform domain. The methods based on discrete cosine transform are more efficient and time saving. However, previously proposed methods in this domain contains a certain number of quality degradations such as blur. Therefore, in this study, a variance based efficient fusion approach has been proposed in discrete cosine transform domain. In terms of performance it has performed better than other approaches.

The most important issue in the architecture design of a fusion system is to accurately evaluate the local content available in a set of input images such as edges, corners, textures, gradients, different focus levels etc. Therefore, Tian et al [45] proposed a statistical based fusion method which exploits the different wavelet coefficients obtained from different focus levels to measure the degree of blur in input images. However, different focus levels provide different distribution of wavelet coefficients. The marginal distribution of wavelet coefficients can be measured using a local adaptive Laplacian mixture. As per study authors, there study has outperformed previously proposed state-of-the-art multi-focus image fusion approaches in terms of visual and quantitative analysis.

Liu et al [46] addressed the issue of multi-focus image fusion in transform domain image fusion. In their study, authors have presented a platform for multi-focus image fusion which combines multi-scale transform and sparse representation techniques. Firstly, they obtained low pass and high pass wavelet coefficients using

multi-scale transform approach. Later, low pass coefficients were combined using sparse representation technique, however, high band coefficients were used to create a composite image using their absolute values as activity level measurement.

2.3 Weight Optimization using Evolutionary Algorithm

Kumar et al [47] proposed a methodology for detection of ductal carcinoma based on image fusion using weight optimization through genetic algorithm. Ductal carcinoma is a deadliest disease in women which spreads exponentially and leads to death in its final stage. The proposed methodology creates an enhanced composite image from a set of X-ray mammography images based on discrete wavelet transform method using genetic algorithm based weight optimization at pixel level weighted average.

Kulkarni et al [48] addressed the problem of multi-focus and multi-spectral image fusion by proposing their approach. In their study, authors have used a genetic algorithm for finding the optimal weights, however, the obtained optimal weights are multiplied with the input source images to create activity maps. Later pixel level fusion is performed to create a visually enhanced optimal image.

Tahir et al [49] presented a novel methodology to address issue of multi-focus image fusion. The said approach consists on multiple steps, first they have implemented genetic algorithm to remove noise from input source images. As a result, input images will become more accurate before image fusion. In the other step, authors have used curvelet transform to decompose input images for fusion.

Kumbhar et al [50] proposed a procedure for the diagnosis of neuro-degenerative signs based on image fusion using weight optimization. Their methodology starts with detection of edges in input source images which were captured using magnetic resonance imaging technique. They have applied morphological filters to fill energy gaps in input images. Later, they generate a feature vectors of five features such as

pixel intensity, location of pixel, wavelet coefficient, histogram of gradient and local binary pattern. However, this feature vector was optimized using evolutionary algorithm such as genetic algorithm for fusion.

Gupta et al [51] addressed the issue of optimization in image fusion. In their methodology, authors have implemented two approaches such as discrete wavelet packet decomposition and intensity hue saturation. First of all, they created a fused image using discrete wavelet packet decomposition technique. Later, they optimize the obtained results using a genetic algorithm. As per the study findings, their methodology has generated better results than technique of intensity hue saturation.

2.4 Critical Analysis

During previous years, a great interest of researchers has been witnessed in the domain of multi-focus image fusion because of its exponentially growing scope. Earlier work in this domain can be classified into two domains such as spatial domain image fusion (section 1.4.1) and transform domain image fusion (section 1.4.2).

Now a day, feature space-based research in the domain of multi-focus image fusion has attained focus of researchers. This kind of fusion methods measure the visibility of input source image in one feature space. The most common example of this work are sparse-representation based method [44], convolution sparse representation method [40], independent component analysis and topographical independent component based method [41], etc. The major objective of these kind of methodologies is to compute a single feature space which can efficiently present visibility of local image patches. Moreover, these methodologies implement the approach of sliding window, which make these methods as shift-invariant.

Most of the previously proposed state-of-the-art methods for spatial domain image fusion estimate clarity of input images on the bases of average of input source image

pixels which introduces undesirable artifacts in a fused image [25]. In earlier years, some novel block based [4] [36] and region based fusion methods [31] [34] [18] [37] have been proposed. The basic principles of block or region-based methods is to select a particular a region or block from input source images on the basis of specific focus measures such as variance, standard deviation, entropy, or spatial frequency etc. However, a selected block or region may contain focused regions along with blurry regions. The resultant fused image might suffer from blocking effect. For region-based methods, it is very hard to obtain stable fusion results, as region-based segmentation of an image is a very difficult task due to irregular boundaries of focused and non-focused regions.

The discussions in this section delineated that most of the earlier techniques have reported promising results in creating an all in focused fused image. In recent studies, the effectiveness of single feature space usage for multi-focus image fusion has been demonstrated. Therefore, there is a pressing need to develop more effective multi-dimensional feature space for characterization of focused and non-focused regions in input source images. The most important contribution of this study is that an ensemble of some local features such as ω_{LBP}, ω_{LO} and ω_{SO} can be employed for better characterization of regions. In general, these features can not only be implemented for region characterization, but can also be employed for extraction of shape and texture-based details to enhance quality of complementary composite fused image. Furthermore, it requires optimal weights to decide contribution of each feature in a fused image. However, the novelty of this work is the usage of weight optimization by genetic algorithm for extraction of maximal spatial details from input source images.

Chapter 3

Image Fusion and Feature Extraction

In order to address raised issues of image fusion in this dissertation, methodology presented in Figure 3.1 is employed. This comprehensive and diversified methodology comprises of multiple steps such as collection of benchmark dataset, feature extraction using local features, weight optimization using genetic algorithm, activity map generation and image fusion etc. For this study, 09 benchmark datasets are collected, where each dataset represents a pair of two images such as left and right focused images, foreground and background focused images. As these datasets are publicly available and contain multi-focus images. Preprocessing is not required in this study, because each pixel of input source image is important for the fusion. Later, three blur segmentation maps are generated for each input image using shape and texture-based local features such as Local Binary Patterns (ω_{LBP}), Sobel Operator (ω_{SO}) and Laplacian Operator (ω_{LO}). Blur segmentation map indicates classification of pixel of an image as focused or non-focused. The optimal weights are obtained using genetic algorithm which decide contribution of each feature in an activity map. By comparing intensity of each pixel of both activity maps (i.e. left and right focused images), a fused image is generated. The effectiveness of a fused image is evaluated in terms of visual and quantitative

analysis using certain statistical and mathematical based quality measures such as Normalized Mutual Information, Average Gradient and Yangs quality metric.

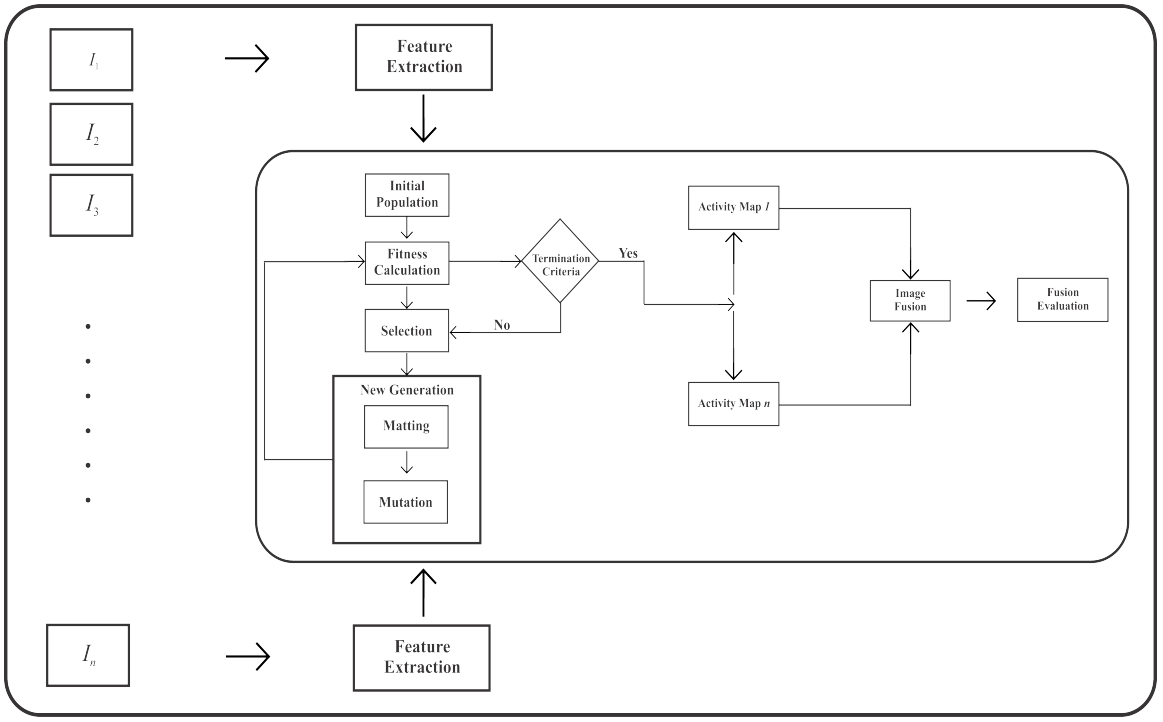

FIGURE 3.1: Generic System Block Diagram.

3.1 Benchmark Dataset

To evaluate effectiveness of this optimal approach, there is a need of a benchmark dataset which should contain multi-focus images of a particular activity or a scene. For this purpose, nine datasets are collected, where each dataset is a pair of two images such as left and right focused, foreground and background focused images. The reason of this selection is two-fold as it contains multi-focus images and it is available publicly.

Figure 3.2 draws a visual interpretation of selected images for evaluation of improved multi-focus image fusion scheme. In this dataset, each pair of images can be labeled using certain titles such as figures a and b are the multi-focus images of a wine bottle. The figures c and d represents diver image, e and f contain a baby image. Likewise, g and h illustrate a fence image. Moreover, i and j are the

multi-focus images of a female model. Furthermore, k, j, m and n are images of product packing and plant. Moreover, figures such as o, p, q and r draw visual illustration of clock and lab images.

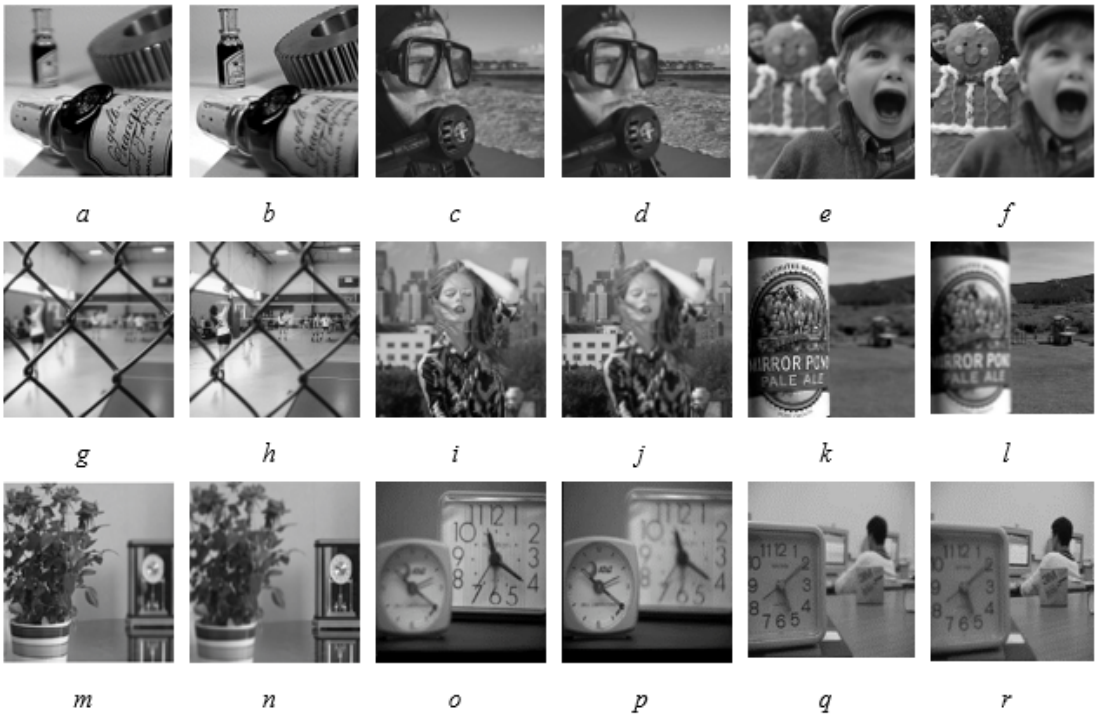

FIGURE 3.2: Visual Illustration of Collected Datasets.

3.2 Feature Extraction Techniques

Feature extraction is a process of extracting certain details from a particular object such as image texture or gradient etc. Feature extraction techniques play a quintessential role in the multi-focus image fusion. The feature extraction techniques extract features from multi-focus images, which are combined into one feature vector, known as a set of features. Later, this set of features can be further refined for fusion.

In the current study, two shape and one texture-based feature extraction techniques are employed from figure 3.3 which are to be titled as Laplacian Operator, Sobel Operator and Local Binary Patterns. To the best of our knowledge, the innovation in this work is that an ensemble of Laplacian Operator, Sobel Operator

and Local Binary Patterns has neither been used earlier with optimized feature weights for the multi-focus image fusion.

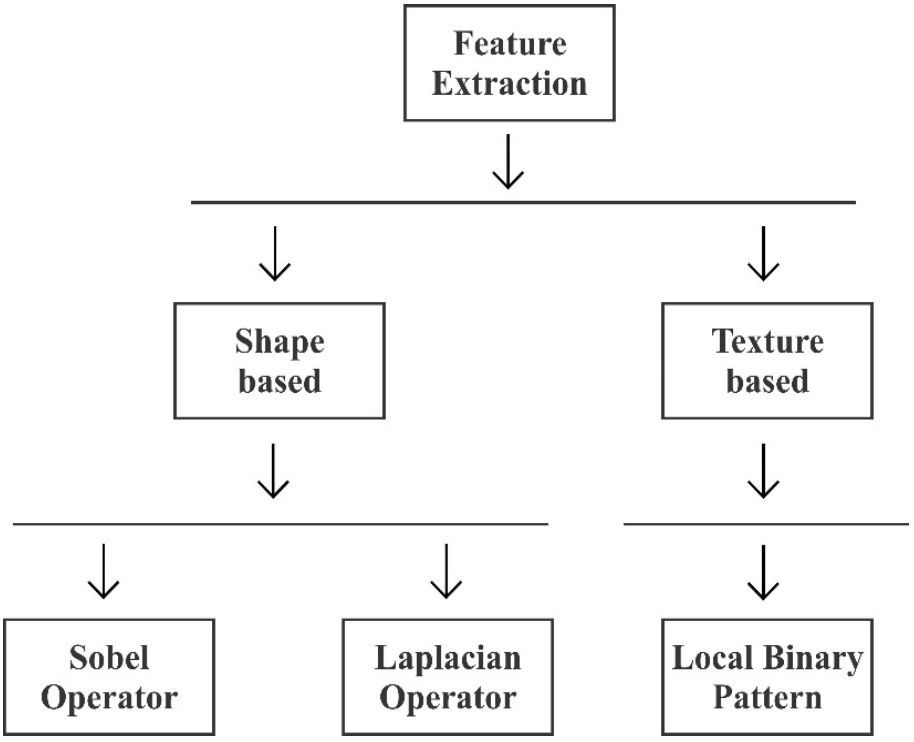

FIGURE 3.3: Classification of Feature Extraction Techniques used in this Study.

3.2.1 Local Binary Patterns

Local Binary Pattern (LBP) is a texture-based feature extraction technique [52]. It was originally proposed for the classification of texture in an image $I(x, y)$. This feature is most commonly used because of its invariance to grey level changes. LBP take a neighborhood values around a pixel such as image block of (3×3) pixels, where it compares the intensity of central pixel with the intensities of its surrounding pixels. If the pixel intensity is greater than or equal to central pixel, then 1 is assigned to a corresponding pixel otherwise 0 is to be assigned. This comparison returns an 8-bit binary sequence, which is to be converted into an equivalent decimal value. The intensity of a central pixel is replaced with a resultant intensity. The intensity of a corresponding pixel is replaced by the intensity of a central pixel of an image block. Similarly, local binary patterns are calculated for all pixels using the sliding window. Obtained binary patterns

are collected in 255 bin histograms; however, the intensity values usually lie in between 0 to 255. Mathematically, LBP can be expressed as equation 3.1.

$$\omega_{LBP} = \sum_{i=0}^{8} f(p_i - p_c) \times 2^n \tag{3.1}$$

$$where f(x) = \begin{cases} 0 & p_c < p_i \\ 1 & p_c \geq p_i \end{cases} \tag{3.2}$$

In equation 3.1, p_c is a central pixel, however, p_i is a neighboring value. The working of LBP is expressed in figure 3.4:

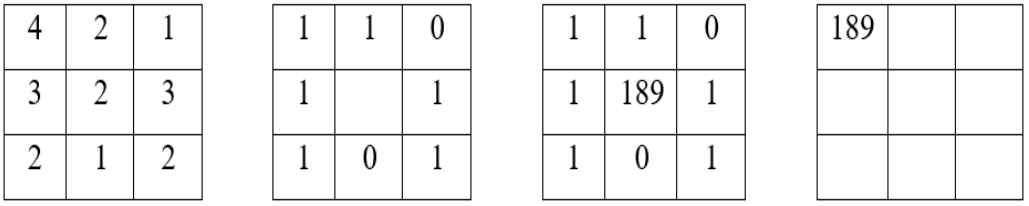

FIGURE 3.4: Working of ω_{LBP} Using a Local Patch Size of 3×3.

A complete algorithm is presented in 1.

Algorithm 1 Local Binary Pattern

INPUT: $I(x, y)$, local patch size of $n \times n$ where $n \mod 2 \neq 0$ AND $n \neq 1$.
OUTPUT: LBP image $\omega_{LBP}(x, y)$.

Read the input image as $I_g(x, y)$.
repeat
Apply an overlapping sliding window, with a block size of $n \times n$.
Take the first image block of nn along with its pixel intensities as $S_w(I_g(n, n))$.
Take the intensity of a central pixel as a threshold T in that particular window.
Compare the intensities of neighboring pixels with T:
if $(p_n(x, y) \geq T)$, return 1.
if $(p_n(x, y) < T)$, return 0.
Return an 8-bit binary code.
Convert 8-bit binary code into decimal.
Replace the value of central pixel, with obtained decimal value.
Collect binary codes in a 255-bin histogram.
until The image is not completely compared.

return Normalized LBP image as $\omega_{LBP}(x, y)$.

3.2.2 Sobel Operator

Sobel operator is a shape-based feature extraction technique [53]. It was originally developed for edge detection in an image $I(x, y)$; however, an edge of an image indicates the most prominent part of changed intensity. It is a gradient based feature extraction method. The Sobel operator takes a neighborhood region R(x,y) of 3×3 around a pixel, where it computes the gradient in x direction and similarly in y direction using equations 3.3 and 3.4. The gradient in x direction can be calculated by convolving the selected region with M_1 using equation 3. The matrix M_1 can expressed as:

$$M_1 = \begin{bmatrix} -1 & 0 & -1 \\ -1 & 0 & -1 \\ -1 & 0 & -1 \end{bmatrix}$$

However, the gradient in y can be calculated by convolving a region with matrix M_2 which can be defined as:

$$M_2 = \begin{bmatrix} -1 & -1 & -1 \\ 0 & 0 & 0 \\ -1 & -1 & -1 \end{bmatrix}$$

This convolution return two gradient matrices F_x and F_y. The total gradient G can be calculated using equation 3.5. A complete algorithm is presented in algorithm 2.

$$F_x(x, y) = R \times M_1 \tag{3.3}$$

$$F_y(x, y) = R \times M_2 \tag{3.4}$$

$$G(x,y) = \sqrt{(F_x)^2 + (F_x)^2} \tag{3.5}$$

$$\theta = tan^{-1}\frac{F_x}{F_y} \tag{3.6}$$

$$\omega_{SO}(x,y) = G(x,y) \tag{3.7}$$

Algorithm 2 Sobel Operator

INPUT: $I(x,y)$, local patch size of $n \times n$ where $n \mod 2 \neq 0$ AND $n \neq 1$.

OUTPUT: SOB image $\omega_{SO}(x,y)$.

Read the input image as $I_g(x,y)$.

repeat

Apply an overlapping sliding window, with a block size of $n \times n$.

Take the first image block of nn along with its pixel intensities as $S_w(I_g(n,n))$.

Estimate the amount of gradient in horizontal direction as $F_x(x,y)$.

Estimate the amount of gradient in vertical direction as $F_y(x,y)$.

Estimate the magnitude of obtained gradients as $G(x,y)$.

Replace the intensity of a central pixel, with obtained magnitude.

Estimate the direction of gradient as $\theta^o \geq \theta \leq 180^o$.

Create a histogram, having nine bins of 20^o each.

Store the obtained magnitude, in the bins of the histogram.

until The image is not completely compared.

return Normalized SOB image as $\omega_{SO}(x,y)$.

3.2.3 Laplacian Operator

Laplacian operator is also a shape-based feature extraction technique [54]. It is developed for the edge detection in an image. As compared with the previously

proposed edge detection techniques such as Sobel Operator, Laplacian operator is a second order partial derivative. Mathematically, Laplacian operator can be expressed in equation 3.8.

$$I'(x,y) = \partial^2(x,y) \times I(x,y) \tag{3.8}$$

Where $\partial^2(x,y)$ is a Laplacian operation over an image $I(x,y)$, it takes a neighboring region such as 3×3 around a pixel, where it convolves the selected region $R(x,y)$ with matrix M_3 using equation 3.9.

$$M_3 = \begin{bmatrix} 1 & 1 & 1 \\ 1 & -8 & 1 \\ 1 & 1 & 1 \end{bmatrix}$$

$$\omega_{LO}(x,y) = R \times M_3 \tag{3.9}$$

This convolution operation returns one large matrix containing a brief detail of edges of an image. A complete algorithm is given in algorithm 3

Algorithm 3 Laplacian Operator

INPUT: $I(x,y)$, local patch size of $n \times n$ where $n \mod 2 \neq 0$ AND $n \neq 1$.

OUTPUT: Laplacian image $\omega_{LO}(x,y)$.

Read the input image as $I_g(x,y)$.

repeat

Apply an overlapping sliding window, with a block size of $n \times n$.

Take the first image block of nn along with its pixel intensities as $S_w(I_g(n,n))$.

Estimate the amount of gradient in $I_g(x,y)$ by using equation 11.

Replace the intensity of a central pixel with the obtained value.

until The image is not completely compared.

return Normalized Laplacian image as $\omega_{LO}(x,y)$.

3.3 Generation of blur segmentation map

Non-focus blur is mostly common in the images, which are captured using photographic sensors. The main reason for this non-focus blur is, that a photographic sensor focuses only on the objects which lie in its focus plane, rest of the portions of an image are blurred or de-focused. Activities such as image restoration, one has to segment the blurred and focused regions of an image. As this study is related to the multi-focus image fusion, the input images are left or right focused. Therefore, a segmentation is performed to separate focused and non-focused regions of an image using previously proposed state-of-the-art algorithm [55] based on shape and texture-based feature extraction techniques. The segmentation algorithm consists on the following steps as follow:

3.3.1 Sharpness Map Generation

In the first step, sharpness maps are generated using shape and texture-based features such as ω_{LBP}, ω_{SO}, ω_{LO}. The sharpness map is calculated for a local patch such as of 3×3 around a pixel.

3.3.2 Alpha map initialization

In the second step, input image pixels are fragmented as focused or non-focused pixel. This fragmentation can be labeled as alpha matting. The image formation can be modeled using equation 3.10:

$$I(x,y) = \alpha_{x,y} \times F(x,y) + (1 - \alpha_{x,y}) \times B(x,y) \tag{3.10}$$

Where $\alpha_{x,y}$ is the opacity value of an image pixel at position (x,y) however, $F(x,y)$ is a focused pixel and $B(x,y)$ refers to a blurred pixel; This process requires a user to mark those pixels as $\alpha = 0$ or $\alpha = 1$. The classification process is initiated automatically with a double threshold using equation 3.11 and returns a

value α for each pixel. In this study, a double threshold can be represented using multiple mathematical symbols such as T_{m_1} and T_{m_2} respectively. However, in scientific literature, there reported values were $T_{m_1} = 0.3$ and $T_{m_2} = 0.01$. For experimentation, same values were selected as they generated best and outstanding results.

$$I(x,y) = \begin{cases} 1 & I(x,y) > T_{m_1} \\ 0 & I(x,y) < T_{m_2} \\ \omega_{LBP}, \omega_{LO}, \omega_{SO} & Otherwise \end{cases} \tag{3.11}$$

In this classification process $I(x,y)$ is a decomposed image containing focused and non-focused image pixels which can be titled as α_{map}. However, 1 is assigned to focused pixels and 0 is to be assigned to de-focused pixels. For instance, if both cases are not selected, then a random value is to be chosen from any of the segmented maps.

3.3.3 Calculation of Alpha map

The alpha map can be calculated using equation 3.12.

$$E(\alpha) = \alpha^T I\alpha + \lambda(\alpha - \hat{\alpha})^T(\alpha - \hat{\alpha}) \tag{3.12}$$

Where α is a vector map of α_{map}, however, I is the alpha matting matrix. The first term in this expression ensures smoothness whereas second indicates information enhancement in an image.

3.3.4 Inference

After estimating α_{map} for multiple images on a local patch size of 3×3, a model was formulated to make an ultimate decision regarding image sharpness and smoothness. The output of this procedure is a map of sharped pixels at a dynamic local

patch size. This algorithm returns a sharpness map in a gray-scale image where a higher pixel intensity indicates a best sharpness.

3.4 Weight optimization using genetic algorithm

3.4.1 Genetic Algorithm

Genetic algorithm is one of the powerful optimization techniques [56] which is adopted from the phenomena of nature. Genetic algorithm makes a simulation of evolution to find the best chromosomes. Unlike, other optimization techniques, genetic algorithm never uses a partial derivative to find a local minimal. Randomness plays a quintessential role in genetic algorithm, which makes it to keep searching the chromosome space for finding a best chromosomes. Figure 3.5 below provides the flow chart of genetic algorithm.

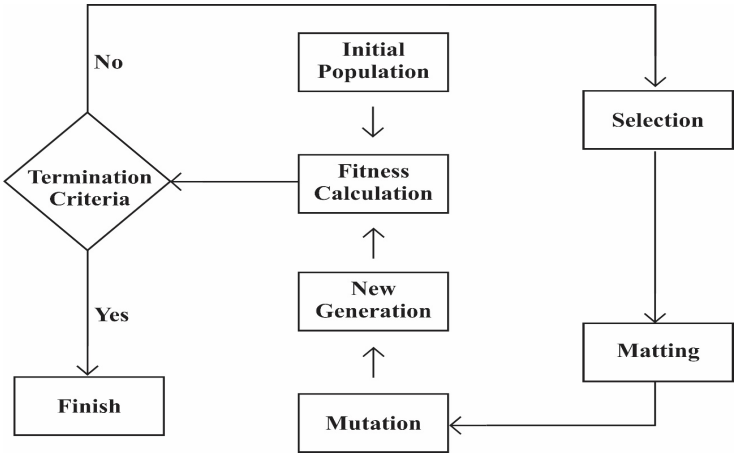

FIGURE 3.5: Flow Diagram of Genetic Algorithm.

Initially, genetic algorithm initiates a population of randomly generated chromosomes. These randomly generated chromosomes are evaluated according to their fitness values. However, a fitness value is a numeric value. If an initial population does not fulfill the termination criteria, then best chromosomes are selected on the basis of higher fitness scores. The first operator of genetic algorithm is selection, where a pair of chromosomes is selected on the basis of higher fitness values. A

Algorithm 4 Genetic Algorithm

```
Initiate a random population of chromosomes.
repeat
  Calculate fitness values of randomly generated chromosomes.
  repeat
    Select best chromosomes using higher fitness values.
    Perform matting using selected parents.
    Perform mutation.
    Compute fitness of new chromosomes.
  until Creation of new population.
until Termination criteria is not fulfilled.

return best chromosome [θ0, θ1, θ2] from best chromosome population.
```

process of matting is performed using a selected pair, where it create two more chromosomes, which replace the non-selected chromosomes in the previous generation. The number of chromosomes is to be same as of previous generation. This sequence of instruction is kept in execution continuously until the termination criteria is not fulfilled.

3.4.2 Initial Population

In the first phase of genetic algorithm, a random population of five chromosomes are generated where each chromosome contains three genes. However, the sum of these genes should exactly be one. The main reason of applying this constraint is that we want to select a best combination of genes, as these weights decide contribution of each feature in an activity map for the image fusion.

3.4.3 Selection

In the second phase, best chromosomes are selected for the next generation on the basis of their fitness scores. However, this selection can be made using certain selection methods such as Roulette Wheel, Fittest Half and Random. In this study, best chromosomes are selected using roulette wheel methodology. Because, in this type of selection method, each chromosome has a chance to be selected

including a chromosome having a lower fitness score. As it is generally observed that sometimes chromosome having a lower fitness score generates outstanding results.

3.4.4 Fitness Function

Fitness function estimates fitness value of a chromosome, how to calculate the fitness function it depends upon the optimization problem. If one want to optimize a function, then a function should be implemented into the fitness function. In this dissertation, the fitness scores are calculated using the image entropy as in equation 3.13.

$$Image\ Entropy = -\sum_{i=0}^{255}(p_i)\log_2(p_i) \tag{3.13}$$

In each generation, there are five chromosomes and each chromosome consist on three genes, where θ_0, θ_1 and θ_2 are the individual genes of each chromosome which decide contribution of each feature in a fused image. Therefore, five images are generated using each chromosome such as $I_{F1}(x,y)$, $I_{F_2}(x,y)$, $I_{F3}(x,y)$, $I_{F_4}(x,y)$ and $I_{F5}(x,y)$ however, each image is evaluated using equation 3.13. The formulation of new images can be modeled using equations 3.14 to 3.16 where ω_{LBP} is a local binary pattern, ω_{LO} is a Laplacian operator and ω_{SO} is a Sobel operator.

$$I_1'(x,y) = \theta_0 \times \omega_{LBP} + \theta_1 \times \omega_{LO} + \theta_2 \times \omega_{SO} \tag{3.14}$$

$$I_2'(x,y) = \theta_0 \times \omega_{LBP} + \theta_1 \times \omega_{LO} + \theta_2 \times \omega_{SO} \tag{3.15}$$

$$I_{Fn}(x,y) = \begin{cases} I_1(x,y) & if I_1'(x,y) \geq I_2'(x,y) \\ I_2(x,y) & Otherwise \end{cases} \tag{3.16}$$

In this experimentation, fitness function is a maximization function because we are interested in studying variations of pixel intensities in input source images. Therefore, chromosome having a maximum entropy score is to selected as a best chromosome.

3.4.5 Matting

Next step of genetic algorithm is matting which is also known as crossover, the crossover can be of multiple types such as single-point crossover and two-point crossover. However, in this study, a procedure of single point crossover is implemented. As a result, two new chromosomes are generated. At this stage, there is a clear chance that sum of each newly created chromosome might be greater or less than one. Therefore, algorithm presented in 5 is implemented for scaling obtained weights.

Algorithm 5 Algorithm for Weight Scaling.

INPUT: Weights Array $C[]$.

OUTPUT: Scaled Weights Array $C[]$.

Read weights array as $C[]$.
$totalsum = sum(C[])$
if $totalsum > 1 \ \ OR \ \ totalsum < 1$ **then**

  while $totalsum \neq 1$ **do**

    for i *in* $range(length(C))$ **do**
      $C[i] = C[i]$ / $totalsum$
    end for
    $totalsum = sum(C[])$
    if $totalsum == 1$ **then**
      break
    end if
  end while
end if

return Scaled Weights as $C[]$.

3.4.6 Mutation

The final operation of genetic algorithm is mutation. The process of mutation is performed to improve the variety of chromosomes in the next generation. The chromosomes selected through elitism are not screened through mutation. The main reason for this constraint is that they are already a best solution. Newly, generated chromosomes are screened through process of mutation, otherwise they are identical alike their parents. The mutation can be performed using multiple methods such as Gauss and Reset etc. However, a mutation is implemented using a methodology of Gauss.

3.4.7 New Generation

Genetic algorithm is a random optimization approach as it enhances a current solution by making random changes. However, It is not guaranteed that it can always generate outstanding results because of its randomness. Therefore parent solutions from last generation are always kept in a new generation to obtain a better solution. At this point, one can create a new population of chromosomes which represent a next generation.

3.4.8 Termination Criteria

On successful creation of a new generation, specific termination criteria can be employed to validate whether a genetic algorithm should produce another generation of chromosomes or it gets halted. Therefore, multiple types of termination criteria can be employed at the same time. If any criteria among all fulfill termination requirements, then a genetic algorithm gets halted. In this study, two termination criteria are employed at the same time; such as a fixed number of iterations and no significant change in chromosomes. In a fixed number of iterations based criteria, a genetic algorithm is kept in execution for a limited number of generations such as 500, 1000, or higher. Similarly, in another case, if there is no significant change in

chromosome generations, then a genetic algorithm can be halted to create another generation.

3.5 Generation of Activity Maps

In this study phase, optimized feature weights are obtained using genetic algorithm as discussed in previous sections. From generated populations of chromosomes, a best population is selected on the basis of its fitness value. From the selected population a best chromosome is to be selected using its fitness score. However, the genes of this chromosomes are used as feature weights θ_0, θ_1 and θ_2 respectively.

Later, shape and texture-based features are estimated from input images such as ω_{LBP}, ω_{LO} and ω_{SO}. This process returns three images for each input image such as $\alpha_{\omega_{LBP_1}}(x,y)$, $\alpha_{\omega_{LO_1}}(x,y)$, $\alpha_{\omega_{SO_1}}(x,y)$ similarly for second input image, $\alpha_{\omega_{LBP_2}}(x,y)$, $\alpha_{\omega_{LO_2}}(x,y)$, $\alpha_{\omega_{SO_2}}(x,y)$ in total there are six activity images for each pair of images. Now, a combined activity map is created using each pixel of segmented maps however, each obtained pixel is assigned a weight of selected gene. The resultant value is a feature score for the activity maps. Mathematically, activity maps can be labeled as $\alpha'_1(x,y)$ and $\alpha'_2(x,y)$. This image formulation is modeled using equation 3.17 and 3.18.

$$\alpha'_1(x,y) = \theta_0 \times \alpha_{\omega_{LBP_1}}(x,y) + \theta_1 \times \alpha_{\omega_{LO_1}}(x,y) + \theta_2 \times \alpha_{\omega_{SO_1}}(x,y) \tag{3.17}$$

$$\alpha'_2(x,y) = \theta_0 \times \alpha_{\omega_{LBP_2}}(x,y) + \theta_1 \times \alpha_{\omega_{LO_2}}(x,y) + \theta_2 \times \alpha_{\omega_{SO_2}}(x,y) \tag{3.18}$$

3.6 Improved Image Fusion Scheme

For implementation of improved fusion scheme, sequence of steps mentioned in figure 3.6 are employed. For convenience, this fusion procedure is presented only

for two input images such as $I_1(x, y)$ and $I_2(x, y)$, however, a generalized algorithm for more than two input images is discussed at the end of this section. From figure 3.5, it can be clearly seen that proposed methodology consists on multiple steps. In the first step, proposed method uses a renowned evolutionary algorithm such as a genetic algorithm to obtain optimal weights i.e. θ_0, θ_1 and θ_2 where $\theta_0 + \theta_1 + \theta_2 = 1$. First of all, a random population of five chromosomes is generated, however, each chromosome is composed of three genes respectively. Later, fitness of each chromosome is evaluated using image entropy as discussed in the earlier section. Each chromosome is ranked according to its fitness values. Top two chromosomes with higher fitness values are selected from population of parent chromosomes, to initiate a process of matting. To produce new offspring, a single point crossover to be performed, as a result two new offsprings are produced and replace the chromosomes ranked on the 3rd and 4th grade. There is a need of a genetic diversity in new offspring, otherwise they are identical as their parents. To introduce a genetic diversity in newly born chromosomes, a process of mutation is initiated, which creates a genetic diversity in the offsprings. To maintain the elitism, parent chromosomes are also dispensed in next generation along with a chromosome having lowest fitness value. Now the new generation is composed of two parent chromosomes, mutated chromosomes and the last one with lower fitness score. The major reason for keeping the chromosome with lower fitness value is that it might produce outstanding offspring in the future generations. The process is kept in execution until a termination criteria is not fulfilled. In the end, we select best population of chromosomes from all generated populations. From best selected population, a chromosome is extracted to obtain optimal weights.

In the second step, LBP image using ω_{LBP}, Laplacian image using ω_{LO} and Sobel image by using ω_{SO} over a pair of input source images $I_1(x, y)$ and $I_2(x, y)$ are calculated which return six segmented activity images such as $\alpha_{\omega_{LBP_1}}(x, y)$, $\alpha_{\omega_{LO_1}}(x, y)$, $\alpha_{\omega_{SO_1}}(x, y)$, similarly for second input image, $\alpha_{\omega_{LBP_2}}(x, y)$, $\alpha_{\omega_{LO_2}}(x, y)$ and $\alpha_{\omega_{SO_2}}(x, y)$ respectively. Using segmented images, two general activity images $\alpha'_1(x, y)$ and $\alpha'_2(x, y)$ are created for each pair of input source images by using

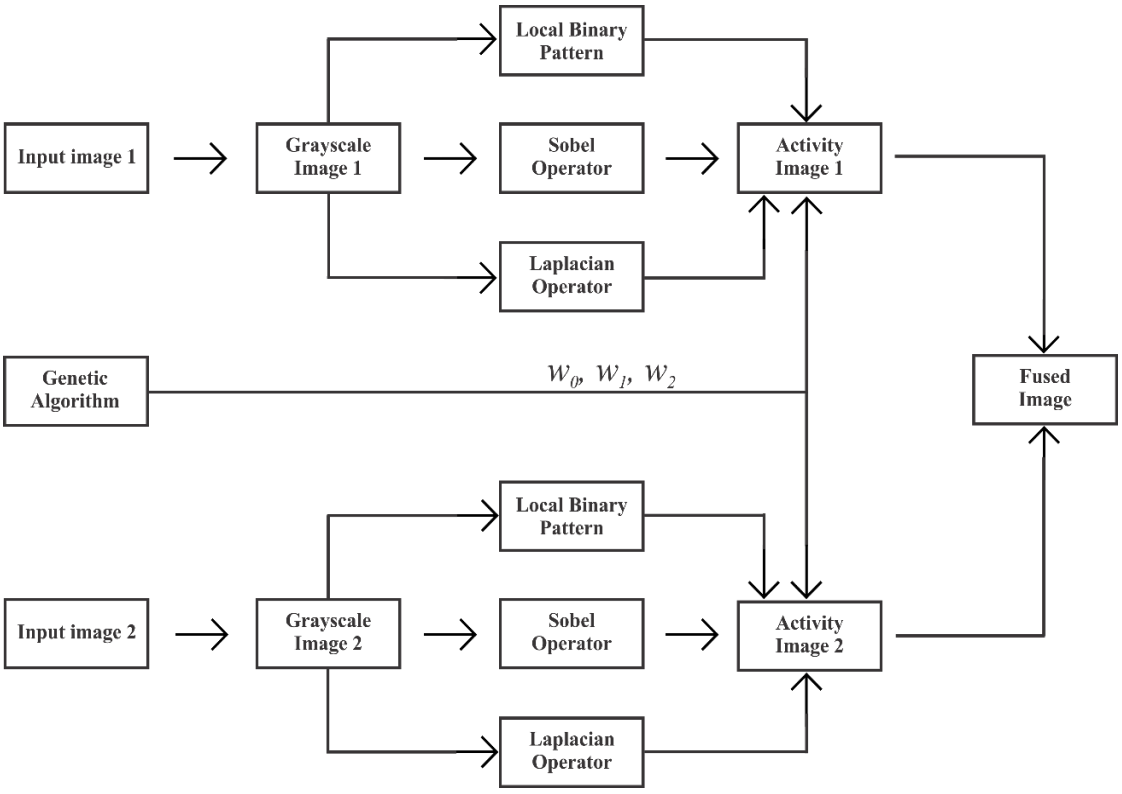

FIGURE 3.6: Block Diagram of Weighted Fusion Methodology using Two Input Images.

equation 3.17 and 3.18, however, obtained values of corresponding pixels to be stored in the newly created two black activity maps.

Here $\alpha_1'(x,y)$ and $\alpha_2'(x,y)$ are the activity maps, which contains focused and non-focused pixels. In the final phase of proposed methodology, the image is fused using activity maps $\alpha_1'(x,y)$ and $\alpha_2'(x,y)$ according to the scheme proposed in equation 3.19.

$$I_F(x,y) = \begin{cases} I_1(x,y) & \alpha_1'(x,y) \geq \alpha_2'(x,y) \\ I_2(x,y) & otherwise \end{cases} \tag{3.19}$$

In equation 3.19, $I_1(x,y)$ and $I_2(x,y)$ are the two input source images. In this step, pixel intensities of both $\alpha_1'(x,y)$ and $\alpha_2'(x,y)$ images are compared. If the pixel intensity of $\alpha_1'(x,y)$ is more than or equal to $\alpha_2'(x,y)$, then a corresponding pixel from $I_1(x,y)$ is registered in a newly created black image at the corresponding index, otherwise a corresponding pixel from $I_2(x,y)$ is to be registered. This

scheme is kept in execution until the complete registration of all corresponding pixels at all corresponding pixels.

Algorithm 6 Genetic Algorithm based Multi-focus Image Fusion using Local Features.

INPUT: $I_m(x, y)$, local patch size of $n \times n$ where $n \mod 2 \neq 0 AND n \neq 1$.
OUTPUT: Fused image $I_F(x, y)$.

Read the input images as $I_m(x, y)$.
$\theta_0, \theta_1, \theta_2$ = execute-Genetic-Algorithm(), where $\theta_0 + \theta_1 + \theta_2 = 1$.
$\alpha_{\omega_{LBP_1}}, \alpha_{\omega_{LO_1}}, \alpha_{\omega_{SO_1}}$ = calculate-Sharpness($I_m(x, y)$).
$\alpha_{\omega_{LBP_2}}, \alpha_{\omega_{LO_2}}, \alpha_{\omega_{SO_2}}$ = calculate-Sharpness($I_{m+1}(x, y)$).
for $i = 0$ *to* *imageheight* **do**

  for $j = 0$ *to* *imagewidth*; **do**
    $\alpha'_1(i, j) = \theta_0 \times \alpha_{\omega_{LBP_1}}(i, j) + \theta_1 \times \alpha_{\omega_{LO_1}}(i, j) + \theta_2 \times \alpha_{\omega_{SO_1}}(i, j)$
    $\alpha'_2(i, j) = \theta_0 \times \alpha_{\omega_{LBP_2}}(i, j) + \theta_1 \times \alpha_{\omega_{LO_2}}(i, j) + \theta_2 \times \alpha_{\omega_{SO_2}}(i, j)$
  end for
end for
for $i = 0$ *to* *imageheight* **do**

  for $j = 0$ *to* *imagewidth*; **do**
    if $(\alpha'_1(i, j) \geq \alpha'_2(i, j))$
    $I_F(i, j) = I_m(x, y)$
    else
    $I_F(i, j) = I_{m+1}(x, y)$
  end for
end for

Chapter 4

Results and Discussions

4.1 Experimental Setup

To find effectiveness of a proposed methodology, multiple experiments are conducted on selected datasets discussed in section 3.1. In this study, shape and texture-based features such as ω_{LBP}, ω_{LO}, ω_{SO} are applied to each dataset to create activity images for fusion. Aforementioned features are implemented using a local patch size of 3×3, 5×5 and 7×7. The working of these feature extraction techniques is briefly discussed in section 3.2.

4.2 Fusion Evaluation

The quality of a fused image can be evaluated using a certain number of statistical quality measures. However, many state-of-the-art quality measures have been proposed in the literature but none of them is better than the other. Therefore, the fused images are evaluated in terms of three quality perspectives such as total preserved edges, mutual information and structural similarity index of input images in a fused image. The selected quality measures are normalized mutual information, average gradient, yang quality metric. Mathematically, these quality measures can be represented as Q_{NMI}, Q_{Y_C} and $G_{(x,y)}^{(AB/F)}$.

4.2.1 Normalized Mutual Evaluation

Mutual information is a statistical measure which is used to estimate distance between two entities such as left and right focused image [57]. This measure uses a cross entropy such as $P(x, y)$ for distance estimation. Mathematically, entropy for an image $I_1(x, y)$ can be defined using equation 4.1 as follow:

$$I_1(x, y) = -\sum_{x,y} P(x, y) \log_2 \frac{P(x, y)}{P(x) \times P(y)} \tag{4.1}$$

Where $P(x, y)$ is a joint probability of x and y in an image, however, x, represents distribution of x in an image, whereas y denotes the distribution of y in an image. Therefore x and y are totally dependent which leads towards zero.

$$P(x, y) = P(x) \times P(y) \tag{4.2}$$

By using equation 4.1

$$I_1(x, y) = -\sum_{x,y} P(x, y) \log_2 \frac{P(x) \times P(y)}{P(x) \times P(y)} \tag{4.3}$$

As $\log_2 = 1$ and $I_1(x, y) = 0$

Similarly, equation 4.4 can be used to evaluate a fused image using input images x and y.

$$M_F^{x,y} = I(F, x) + I(F, y) \tag{4.4}$$

Where $I(F, x)$ indicates the mutual information between fused image F and input image x. The other term is a mutual information between F and other input image y. Now, normalized mutual information between two images can be calculated as follow:

$$NMI = \frac{I(x,y)}{max\{H(x)+H(y)\}} \tag{4.5}$$

On the basis of equation 4.4, NMI can be estimated between fused image and input images using equation 4.5.

$$NMI = \frac{I(F,x)}{H(F)+H(x)} + \frac{I(F,y)}{H(F)+H(y)} \tag{4.6}$$

In 4.6, x and y are the input images and F is a fused image.

The terms of equation 4.6 can be calculated as follows:

$$H(F) = \sum_{i=0}^{255} P_i(F) \log_2 P_i(F) \tag{4.7}$$

$$H(x) = \sum_{i=0}^{255} P_i(x) \log_2 P_i(x) \tag{4.8}$$

$$H(y) = \sum_{i=0}^{n} P_i(y) \log_2 P_i(y) \tag{4.9}$$

$$I(F,x) = H(x) - H(x|F) \tag{4.10}$$

$$I(F,y) = H(y) - H(y|F) \tag{4.11}$$

$$H(x|F) = -\frac{1}{2}H(x) + H(F) \tag{4.12}$$

$$H(y|F) = -\frac{1}{2}H(y) + H(F) \tag{4.13}$$

4.2.2 Gradient Based Fusion Evaluation

The major goal of image fusion is to preserve all extracted information from input images to a one single fused image. Therefore, a fusion scheme should measure accurate amount of extracted information from input images and also measure its capability to transfer the information as accurately as possible. The quantity of edges information which is being transferred to a fused image from a set of input images can be calculated using this measure [58]. Lets consider the two input images $I_1(x, y)$, $I_2(x, y)$ and a fused image $F(x, y)$.

The total amount of edges in $I_1(x, y)$, $I_2(x, y)$ and $F(x, y)$ can be evaluated using equation 4.14 to 4.16.

$$G'_A(x, y) = \frac{\partial I_1}{\partial x} + \frac{\partial I_1}{\partial y} \tag{4.14}$$

$$G'_B(x, y) = \frac{\partial I_2}{\partial x} + \frac{\partial I_2}{\partial y} \tag{4.15}$$

$$G'_F(x, y) = \frac{\partial I_F}{\partial x} + \frac{\partial I_F}{\partial y} \tag{4.16}$$

Where $G'_A(x, y)$, $G'_B(x, y)$ and $G'_F(x, y)$ indicate the amount of edges available in $I_1(x, y)$, $I_2(x, y)$ and $I_F(x, y)$. However, the partial derivative of an input image such as $\frac{\partial I_1}{\partial x}$ with respect to x, returns information of horizontal edges. Similarly, $\frac{\partial I_1}{\partial y}$ evaluates amount of vertical edges. The equations 34 35 return two large images containing horizontal and vertical edges. There is a need of a single image which should contain both type of edges such as horizontal and vertical edges, therefore, there is a need to apply equations of 4.17 4.19 as follow.

$$G'_A(x, y) = \sqrt{\frac{\partial I_1}{\partial x}^2 + \frac{\partial I_1}{\partial y}^2} \tag{4.17}$$

$$G'_B(x,y) = \sqrt{\frac{\partial I_2}{\partial x}^2 + \frac{\partial I_2}{\partial y}^2} \tag{4.18}$$

$$G'_F(x,y) = \sqrt{\frac{\partial I_F}{\partial x}^2 + \frac{\partial I_F}{\partial y}^2} \tag{4.19}$$

Equations 4.17 4.19 return three resultant images. Transferred amount of edges from $I_1(x,y)$ to $F(x,y)$ and $I_2(x,y)$ to F(x,y) can be estimated using equation 4.20 and 4.21 as follow:

$$G^{A,F}_{(x,y)} = \begin{cases} \frac{G'_F(x,y)}{G'_A(x,y)} & if G'_A(x,y) > G'_F(x,y) \\ \frac{G'_A(x,y)}{G'_F(x,y)} & otherwise \end{cases} \tag{4.20}$$

$$G^{B,F}_{(x,y)} = \begin{cases} \frac{G'_F(x,y)}{G'_B(x,y)} & if G'_B(x,y) > G'_F(x,y) \\ \frac{G'_B(x,y)}{G'_F(x,y)} & otherwise \end{cases} \tag{4.21}$$

Now there are two images such as $G^{A,F}_{(x,y)}$ and $G^{B,F}_{(x,y)}$, the output should be a single image $G^{(AB/F)}_{(x,y)}$ with effective edges information extracted from $I_1(x,y)$, $I_2(x,y)$ and $I_F(x,y)$. Therefore, there is a need to apply the last mathematical model as mentioned in equation 4.22.

$$G^{(AB/F)}_{(x,y)} = \frac{G^{A,F}_{x,y} \times G'_A(x,y) + G^{B,F}_{x,y} \times G'_B(x,y)}{G'_A(x,y) + G'_B(x,y)} \tag{4.22}$$

However, one single value can be obtained by taking the average of $G^{(AB/F)}_{(x,y)}$. As it is also one large image.

4.2.3 Similarity Based Fusion Evaluation

The structure similarity index metric (SSIM) is a statistical based fusion evaluation measure. This metric distinguishes conflicting/complementary regions from

redundant regions in an input source image using SSIM [59]. Mathematically, SSIM can be defined as equation 4.23 as follow:

$$SSIM(x,y) = \frac{(2w_x\bar{w}_y + c_1)(2\sigma_{w_xw_y} + c_2)}{(\bar{w_x}^2 + \bar{w_y}^2 + c_1)(\sigma^2_{w_x} + \sigma^2_{w_y} + c_2)} \tag{4.23}$$

The equation 4.23 can be further simplified as follow:

$$SSIM(x,y) = \frac{(2\bar{w}_x\bar{w}_y + C_1)(2\sigma_{w_xw_y} + C_2)(\sigma_{w_xw_y} + C_3)}{(w^2_x + w^2_y + C_1)(\sigma^2_{w_x} + \sigma^2_{w_y} + C_2)(\sigma_{w_x}\sigma_{w_y} + C_3)} \tag{4.24}$$

where C_1, C_2 and C_3 are constants values with $C_3 = \frac{C_2}{2}$, $\bar{w}_x$ and $\bar{w}_y$ are means of input images x and y. Similarly, σ_{w_x} and σ_{w_y} are variance scores of input images, however, $\sigma_(w_xw_y)$ represents covariance of both input source images. To evaluate a particular fused image using this quality metric, SSIM can be estimated using equations below:

$$SSIM(A,F) = \frac{(2\bar{w}_A\bar{w}_F + C_1)(2\sigma_{w_Aw_F} + C_2)(\sigma_{w_Aw_F} + C_3)}{(w^2_A + w^2_F + C_1)(\sigma^2_{w_A} + \sigma^2_{w_F} + C_2)(\sigma_{w_A}\sigma_{w_F} + C_3)} \tag{4.25}$$

$$SSIM(B,F) = \frac{(2\bar{w}_B\bar{w}_F + C_1)(2\sigma_{w_Bw_F} + C_2)(\sigma_{w_Bw_F} + C_3)}{(w^2_B + w^2_F + C_1)(\sigma^2_{w_B} + \sigma^2_{w_F} + C_2)(\sigma_{w_B}\sigma_{w_F} + C_3)} \tag{4.26}$$

$$SSIM(A,B) = \frac{(2\bar{w}_A\bar{w}_B + C_1)(2\sigma_{w_Aw_B} + C_2)(\sigma_{w_Aw_B} + C_3)}{(w^2_A + w^2_B + C_1)(\sigma^2_{w_A} + \sigma^2_{w_B} + C_2)(\sigma_{w_A}\sigma_{w_B} + C_3)} \tag{4.27}$$

$$Q(A,B,F) = \begin{cases} \lambda(w)SSIM(A,F)(1-\lambda(w))SSIM(B,F), & if\ SSIM(A,B) \geq 0.75 \\ max\{SSIM(A,F), SSIM(B,F)\}, & if\ SSIM(A,B) < 0.75 \end{cases} \tag{4.28}$$

where $\lambda(w)$ is a local weight, which is calculated using equation 4.29

$$\lambda(w) = \frac{V(A)}{V(A) + V(B)} \tag{4.29}$$

4.3 Fusion Results

In this study, multiple experiments are being conducted to obtain best results of image fusion. The image fusion is performed using a certain number of shape and texture-based features such as ω_{LBP}, ω_{LO}, ω_{SO}. These techniques are applied and verified over selected datasets and obtained multiple activity maps for image fusion. Later, these activity maps were combined using optimal weights which were obtained through an evolutionary algorithm such as genetic algorithm and the combined activity maps are used to restore a particular image. The list of performed experiments can be described as follow:

4.3.1 Effect of Blur on Image Texture

The first experiment is related to the effect of blur on image texture. Therefore, a vigorous investigation is conducted to evaluate impact of different blur magnitudes on image texture. This experimentation is performed over a selected set of input images such as a road image and snipper image using blur radiuses β_r of 0.25, 0.5, 0.75 and 1.0. The effectiveness of this experiment is evaluated using statistical measures of standard deviation and variance.

To study variations of quality degradations in image texture over multiple blur magnitudes β_r, an experimentation is conducted over a selected set of input images. To identify texture in an input image, a texture-based operator such as ω_{LBP} is applied using a local patch size of 33. The obtained image is blurred in five iterations of $\beta_r = 0.0, 0.25, 0.50, 0.75, 1.0$ to obtain degraded image textures as $D_{T_0}(x, y)$, $D_{T_1}(x, y)$, $D_{T_2}(x, y)$, $D_{T_3}(x, y)$ and $D_{T_4}(x, y)$, however, each obtained image is evaluated in each iteration.

Figure 4.1 below, draws an illustration of texture degradations in road image over multiple blur magnitudes. In figure 1(a), original input image of road is presented. Figure 1(b), illustrates image texture at $\beta_r = 0$, however, figures 1(c) to 1(f) present texture degradations at $\beta_r = 0.25.\ 0.50, 0.75, 1.0$. The evaluation of these degradations is illustrated in figures 1(g) and 1(h) using standard deviation and variance respectively. From figures it can be observed that there is no degradation in image texture in between $\beta_r = 0.0$ and $\beta_r = 0.25$ as obtained results are closer which indicate that ω_{LBP} is robust to small amount of blur. However, on other blur magnitudes, a significant degradation is observed in image texture. The results indicate that a texture degradation is directly proportional to a greater blur magnitude.

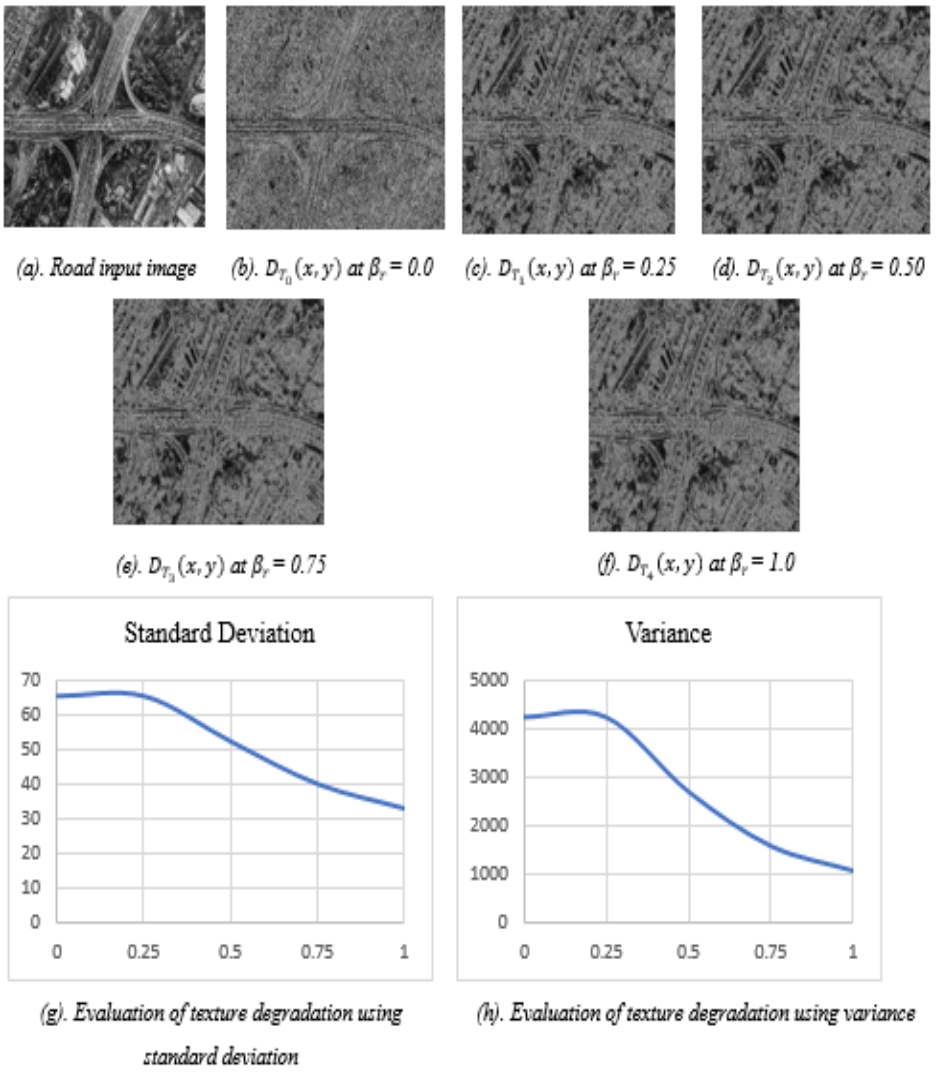

FIGURE 4.1: Evaluating Effect of Blur on Image Texture using Road Image.

Figure 4.2 presents texture degradations in a snipper image over different blur radiuses. The original input image of a snipper is illustrated in figure 2(a). Figure 2(b), contain classified image texture at $\beta_r = 0$, however, the texture degradations on $\beta_r = 0.25$. 0.50, 0.75, 1.0 is illustrated in figures 2(c) to 2(f). The performance of these degradations is presented using figures of 1(g) and 1(h) using variance and standard deviation respectively. It is evident from figures, there is no significant degradation in image texture in between $\beta_r = 0.0$ and $\beta_r = 0.25$ as obtained results are closer. However, other blur radiuses presented significant degradation in image texture.

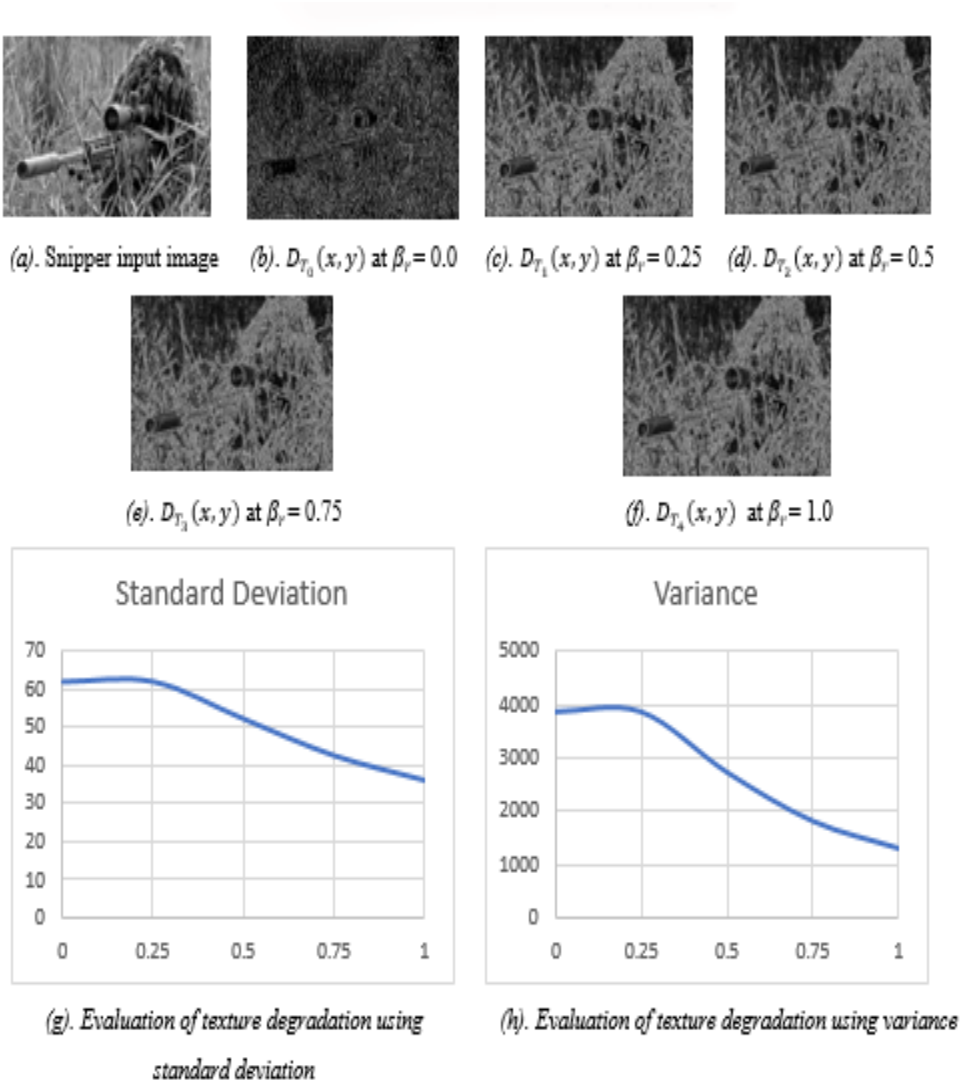

FIGURE 4.2: Evaluating Effect of Blur on Image Texture using Snipper Image.

The discussion in this section shows a relationship graphs of standard deviation

and variance with overall consistency of a texture over a certain amount of blur. The major reason of evaluating this relationship is that a blur directly effects consistency of a texture. However, it is also evident from the obtained scatter plots, that texture is significantly degraded when the amount of blur increases because regions of an image get smoother over a significant increase in blur magnitude.

4.3.2 Effect of Blur on Shape using Laplacian Operator

The second part of first experiment is related to the effect of blur on object edges in an input image. Therefore, another experimentation is conducted to evaluate significant impact of multiple blur magnitudes on image edges. This experimentation is performed over two selected images such as a road image and snipper image by employing blur radiuses β_r of 0.25, 0.5, 0.75 and 1.0. The statistical measures of standard deviation and variance are used to evaluate its effectiveness.

To study variations of degradations in image edges using multiple blur magnitudes β_r, an experimentation is conducted over a selected set of input images. To classify edges in an input image, a second order derivative-based shape operator such as ω_{LO} is applied using a local patch size of 33. Later, obtained image is blurred in five iterations of $\beta_r = 0.0, 0.25, 0.50, 0.75, 1.0$ to obtain degraded image edges as $D_{E_0(x,y)}$, $D_{E_1(x,y)}$, $D_{E_2(x,y)}$, $D_{E_3(x,y)}$ and $D_{E_4(x,y)}$, however, each obtained image with degraded edges is evaluated in each iteration.

Figure 4.3, contains variations of edge degradations in a road image over multiple blur magnitudes. The original road image of road is illustrated in figure 3(a). The effect of blur on image edges at $\beta_r = 0$ is presented in figure 3(b), however, edges degradations at $\beta_r = 0.25.\ 0.50, 0.75, 1.0$ is dispensed in figures 3(c) to 3(f). The evaluation of these degradations is performed in figures of 3(g) and 3(h) using standard deviation and variance respectively. From obtained scatter plots a significant degradation is observed in image edges, as consistency of edges is decreasing significantly. The results indicate that edges degradation is directly proportional to blur magnitude.

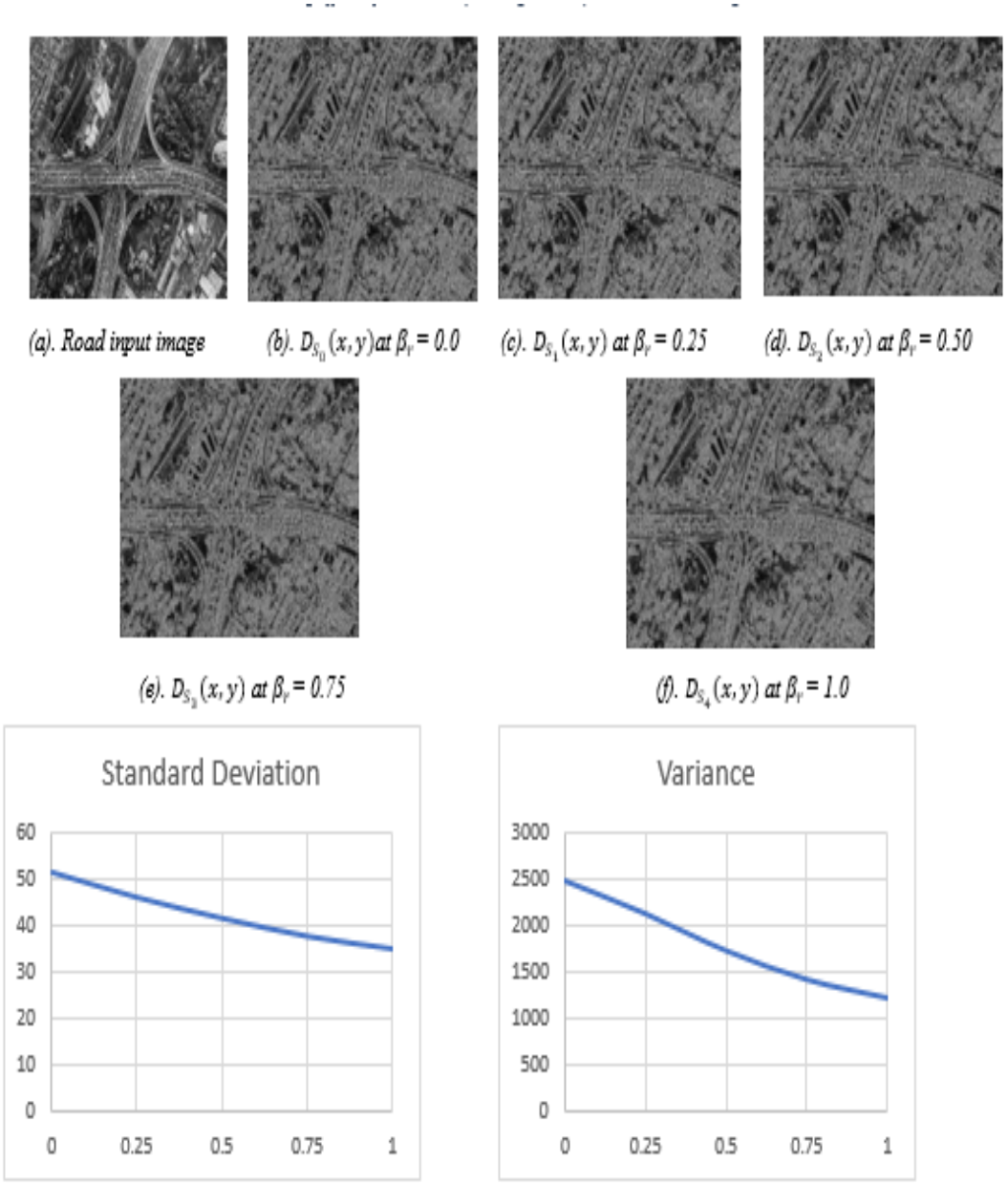

FIGURE 4.3: Evaluating Effect of Blur on Shape using Laplacian Operator on Road Image.

Figure 4.4 presents variations of edges degradations in a snipper image over multiple blur radiuses. Figure 3(a) contains an original road image. The impact of blur on image edges at $\beta_r = 0$ is illustrated in figure 3(b), however, variation of edges degradations on $\beta_r = 0.25$. 0.50, 0.75, 1.0 is presented in figures 3(c) to 3(f). The degradations are studied using standard deviation and variance which is dispensed using figures of 3(g) and 3(h) respectively. These two scatter plots show a strong degradation n image edges, as consistency of edges is decreasing significantly.

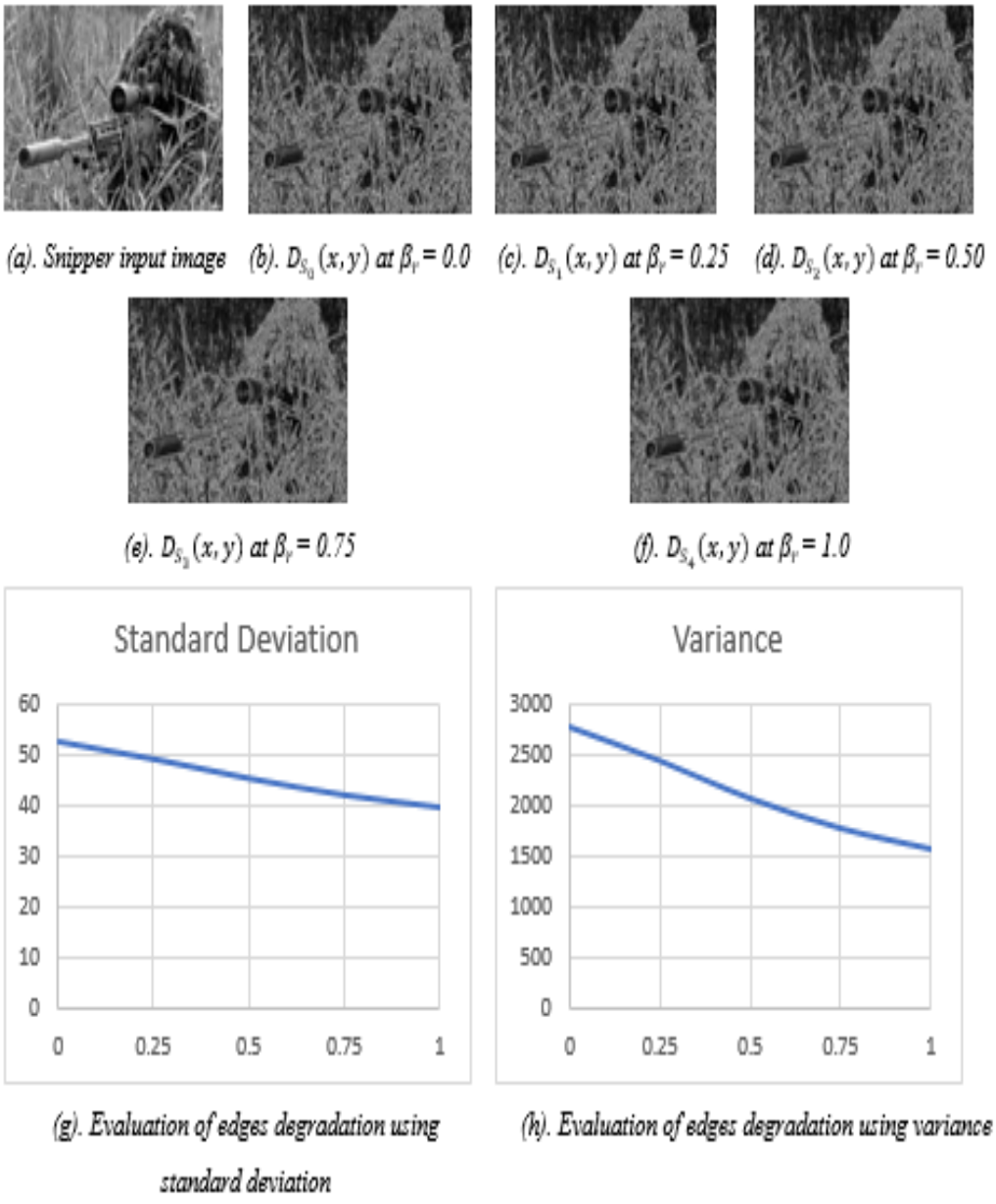

FIGURE 4.4: Evaluating Effect of Blur on Shape using Laplacian Operator on Snipper Image.

The discussions in this module delineate an effective relationship between edges consistency and amount of blur. It presents an association curves of standard deviation and image variance with overall consistency of edges in an image. The reason of finding this relationship is that a blur compromises the consistency of edges in an input image. However, it can be visualized from obtained curves, that edges information decreases when the amount of blur increases. Because smoothness increases over significant increase in blur.

4.3.3 Effect of Blur on Shape using Sobel Operator

The last part of aforementioned experiment is related to the blur effect on object edges in a sobel image. Therefore, this experimentation is conducted to evaluate a significant role of different blur magnitudes on image edges. The experimentation is performed using road and snipper images by taking blur radiuses $_r$ of 0.25, 0.5, 0.75 and 1.0. The effectiveness of this activity is evaluated using statistical measures of standard deviation.

Detecting a particular edge in an input image employs a variety of multiple statistical and mathematical model based procedures which aim at classifying relevant points in a relevant input image where a brightness is changed significantly or, more formally, has multiple loopholes. A set of points in an input image where brightness changes quintessentially are generally referred as a pool of curved line segment based edges. In case of estimating loopholes in a single channel image is referred as a step detection and resolving image signal loopholes in a unit time can be titled as detecting a change in pixel intensity. However, finding a relevant edge is a general requirement in processing an input image for multiple appliances such as machine vision, furthermore, it has been proven effective for extraction and detection of a relevant feature.

To study loss of edges information over multiple blur magnitudes $_r$, an experimentation is conducted over selected input images. To classify edges in an input image, a first order derivative-based shape operator such as ω_{SO} is employed using a local patch size of 33. Later, sobel image is blurred in five iterations of β_r = 0.0, 0.25, 0.50, 0.75, 1.0 to obtain degraded edges information as $D_{S_0(x,y)}$, $D_{S_1(x,y)}$, $D_{S_2(x,y)}$, $D_{S_3(x,y)}$ and $D_{S_4(x,y)}$, however, each degraded image is evaluated in each iteration.

Figure 4.5, contains variations of edge degradations in a road image over multiple blur radiuses. The original image of road is illustrated in figure 5(a). The effect of blur on image edges at $\beta_r = 0$ is presented in figure 5(b), however, edges degradations at $\beta_r = 0.25.$ 0.50, 0.75, 1.0 is dispensed in figures 5(c) to 5(f).

The evaluation of these degradations is performed in figures of 5(g) and 5(h) using standard deviation and variance respectively. These scatter plots present a significant degradation in image edges, as consistency of edges is decreasing significantly. The results indicate that edges degradation is directly proportional to blur magnitude.

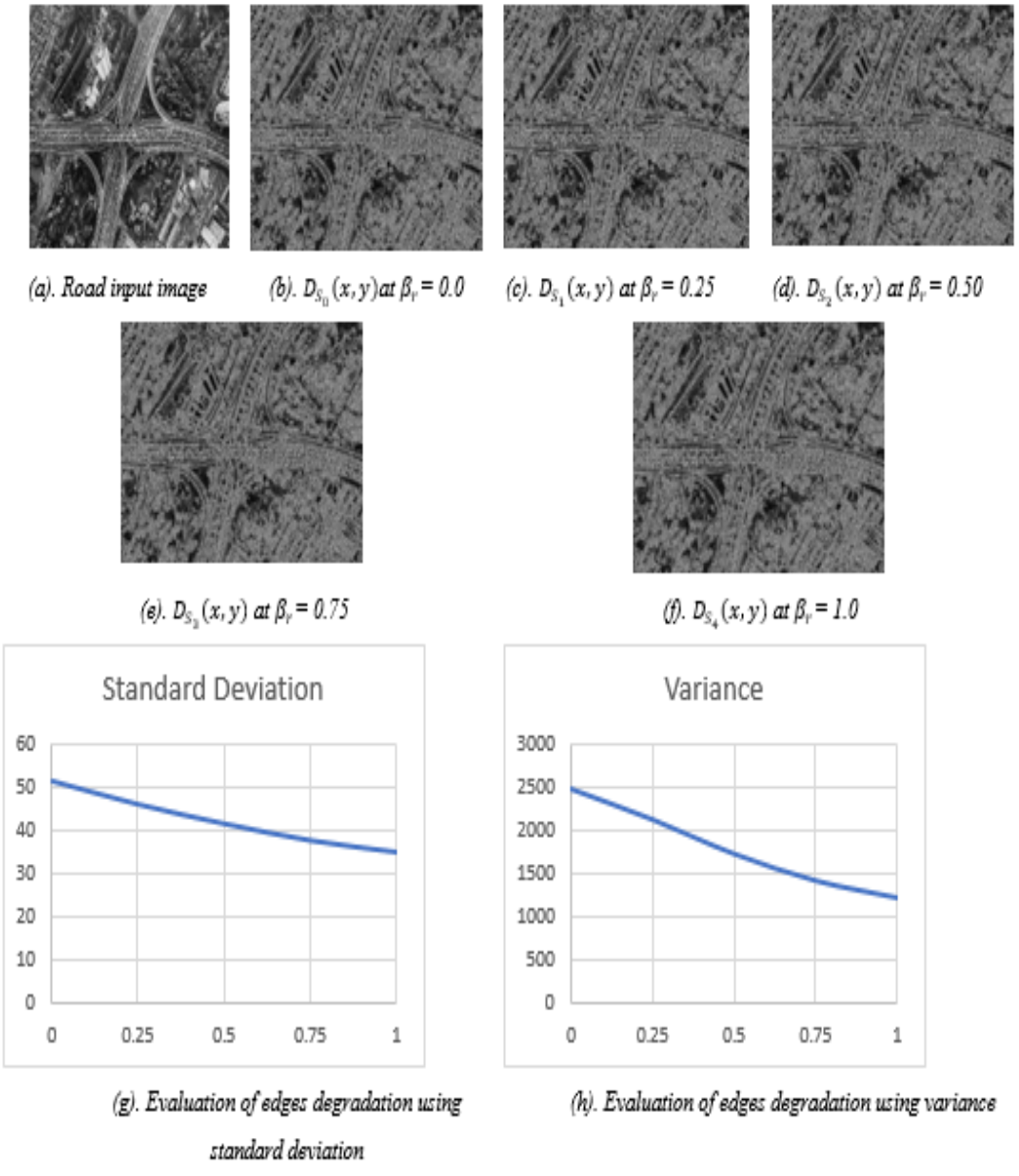

FIGURE 4.5: Evaluating Effect of Blur on Shape using Sobel Operator on Road Image.

Figure 4.6 presents edge degradations in a snipper image over multiple blur magnitudes. The original snipper image of road is presented in figure 6(a). The effect

of blur on image edges at $\beta_r = 0$ is illustrated in figure 6(b), however, edges degradations at $\beta_r = 0.25.$ 0.50, 0.75, 1.0 are presented in figures 6(c) to 6(f). The evaluation of these degradations is performed in figures of 6(g) and 6(h) using standard deviation and variance respectively. These scatter plots indicate a significant degradation in image edges, as consistency of edges is decreasing significantly. The results indicate that edges degradation is directly proportional to blur magnitude because image smoothness increases when significantly blur magnitude increases.

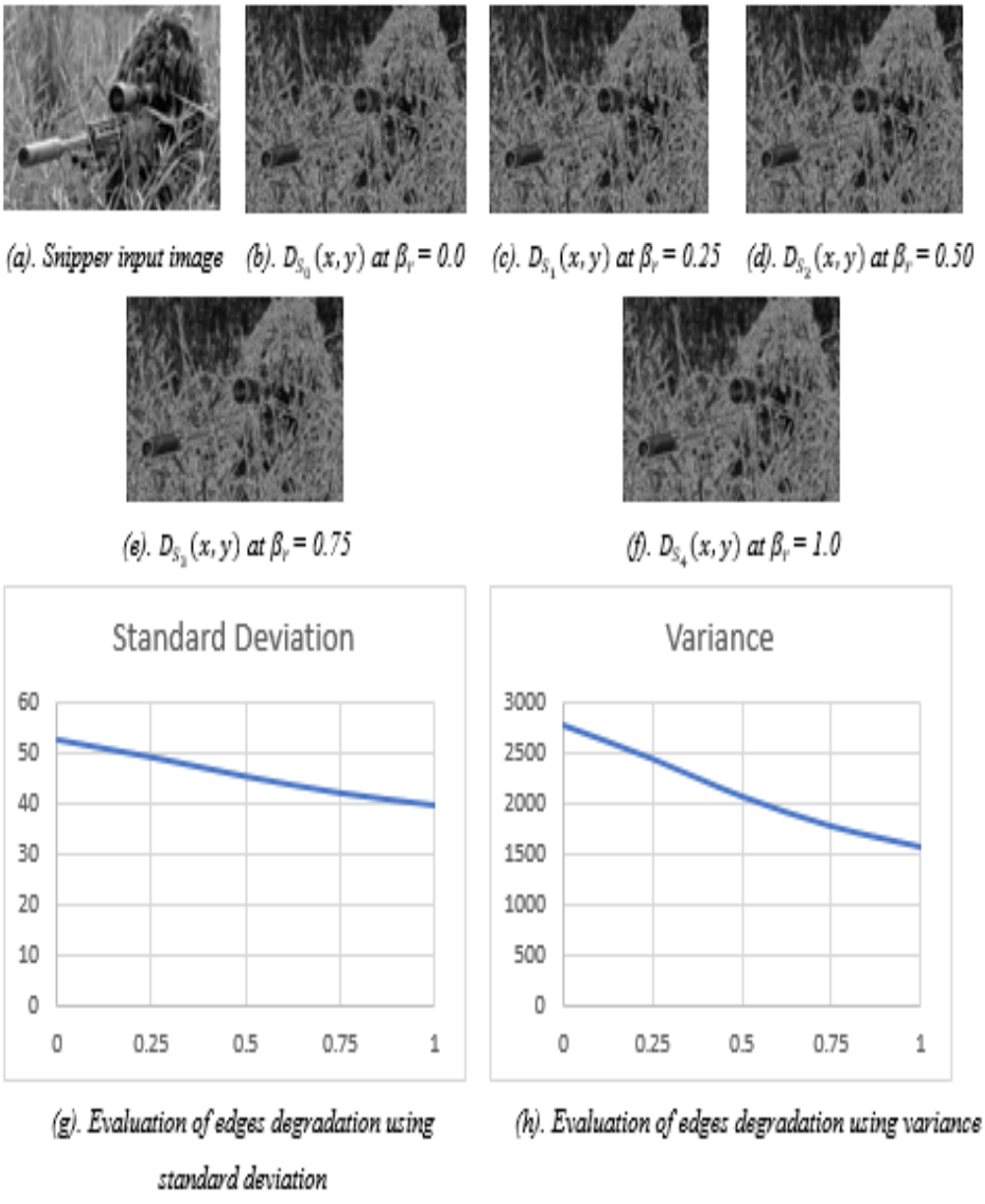

FIGURE 4.6: Evaluating Effect of Blur on Shape using Sobel Operator on Snipper Image.

4.3.4 Objective Evaluation of Fused Images

In this section, a fused image is evaluated using two methods such as qualitative method and quantitative method.

4.3.4.1 Visual Evaluation of Fused Images

The qualitative evaluation of a proposed fusion methodology is performed by comparing graphical quality of fused images. In this section, a comparison of graphical quality of results produced by proposed scheme with state-of-the-art methods. The graphical comparison is performed using four images such as bottle image, child image, fence image and girl image. However, each image contains multiple types details.

Figure 4.7 presents a comparison of proposed fusion scheme with previous state-of-the-art fusion schemes on fence image. The discrete cosine transform based methodologies such as DCHWT, DCTLP, DCTV presents ringing artifacts around fence edges. PCA based methodology is not shrill. Rest of the techniques, contain distorted regions and blur artifacts around fence edges. The results produced by proposed scheme are better than previous methods.

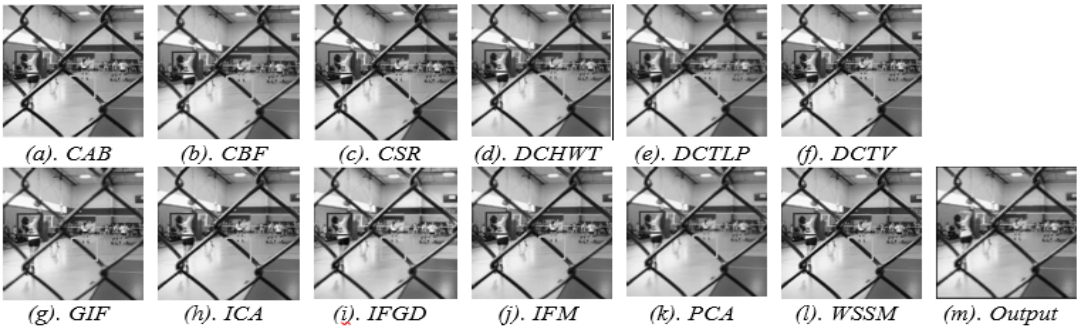

FIGURE 4.7: Graphical Comparison of Fence Image with Previous Fusion Methods.

Figure 4.8 contains a comparison of previous fusion methodologies with proposed fusion methodology on girl image. The input images contain background and foreground focused regions. The DCT based methodologies of DCHWT, DCTLP,

DCTV dispensed ringing artifacts around shoulder of a girl and buildings in background. The methodology of PCA is not shrill. Other techniques are suffering from blur artifacts at aforementioned regions. As compared with previous methods, this methodology is performing better.

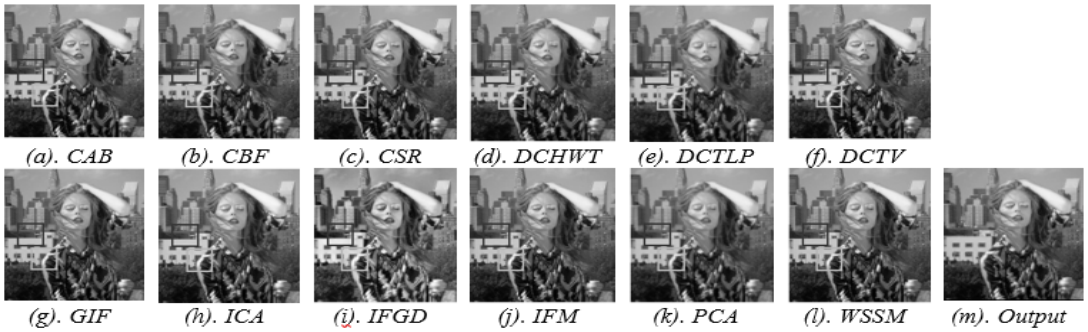

FIGURE 4.8: Graphical Comparison of Girl Image with Previous Fusion Methods.

Figure 4.9 presents a graphical comparison of proposed fusion methodology with previously proposed methodologies on bottle image. The input images contain background and foreground focused regions. Discrete cosine transform based methodologies such as DCHWT, DCTLP, DCTV presented ringing artifacts at multiple locations. PCA based methodology also presented ringing artifacts. It is evident from figures that other approaches are suffering from blur artifacts at background and foreground regions. In a comparison with other methods, this methodology has presented outstanding results on bottle image.

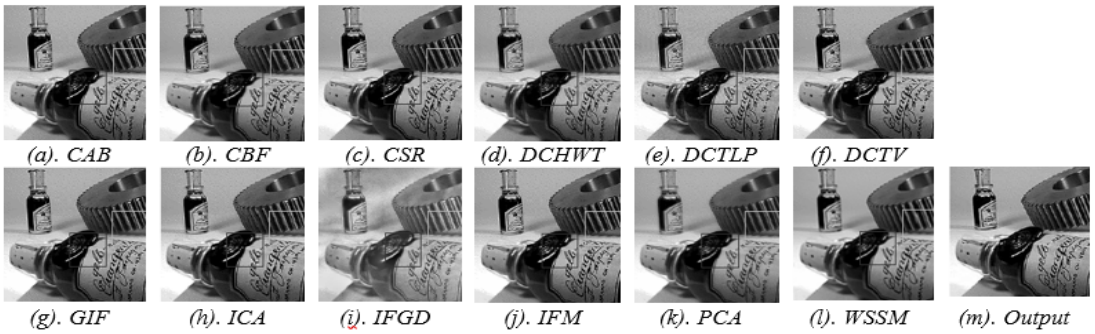

FIGURE 4.9: Graphical Comparison of Bottle Image with Previous Fusion Methods.

Figure 4.10 illustrates comparison results of proposed fusion methodology with previously proposed state-of-the-art methodologies on child image. The input images contain background and foreground focused regions on girl and child objects. The Discrete cosine transform based methodologies such as DCHWT, DCTLP, DCTV presented ringing artifacts at multiple locations in background. The results obtained from PCA based fusion methodology are not sharp. It is evident from figures that other approaches are suffering from blur artifacts at background and foreground regions. In a comparison with other methods, this methodology has presented best results on bottle image.

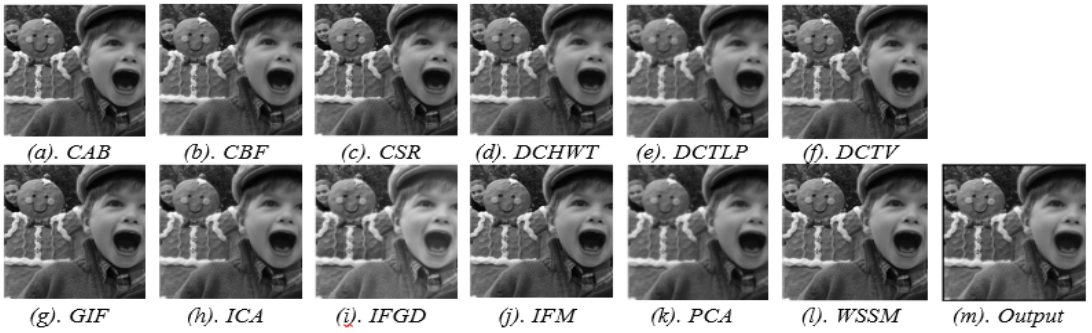

FIGURE 4.10: Graphical Comparison of Child Image with Previous Fusion Methods.

However, figures 4.11 - 4.19 present visual experimental results on other input images such as wine bottle image, diver image, child image, fence image, female model image, product packing image, plant image, clock image and lab image. For this experimentation, the optimal weights are obtained using a genetic algorithm which decide contribution of a relevant feature. In obtained optimal weights, a higher weight indicates a high contribution of a particular feature. Similarly, a lower weight leads towards low contribution.

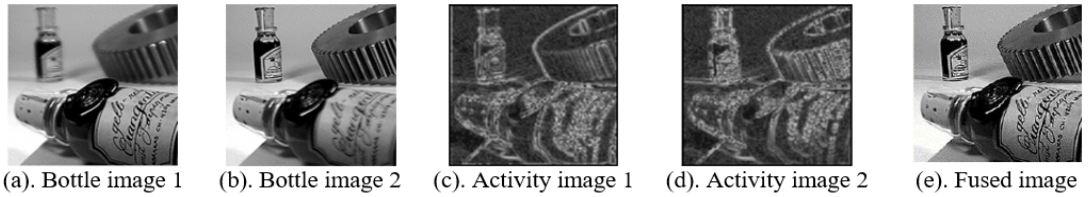

FIGURE 4.11: Experimental Results using Lab Image with Optimal Weights.

(a). Diver image 1 (b). Diver image 2 (c). Activity image 1 (d). Activity image 2 (e). Fused image

$W_{3\times3}$ = [0.41, 0.46, 0.13] $W_{5\times5}$ = [0.32, 0.25, 0.43] $W_{7\times7}$ = [0.40, 0.47, 0.13]

FIGURE 4.12: Experimental Results using Diver Image with Optimal Weights.

(a). Baby image 1 (b). Baby image 2 (c). Activity image 1 (d). Activity image 2 (e). Fused image

$W_{3\times3}$ = [0.43, 0.35, 0.22] $W_{5\times5}$ = [0.40, 0.31, 0.29] $W_{7\times7}$ = [0.21, 0.64, 0.15]

FIGURE 4.13: Experimental Results using Baby Image with Optimal Weights.

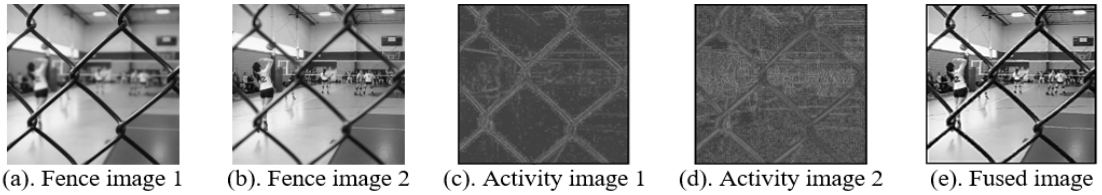

(a). Fence image 1 (b). Fence image 2 (c). Activity image 1 (d). Activity image 2 (e). Fused image

$W_{3\times3}$ = [0.28, 0.23, 0.49] $W_{5\times5}$ = [0.54, 0.35, 0.11] $W_{7\times7}$ = [0.24, 0.10, 0.66]

FIGURE 4.14: Experimental Results using Fence Image with Optimal Weights.

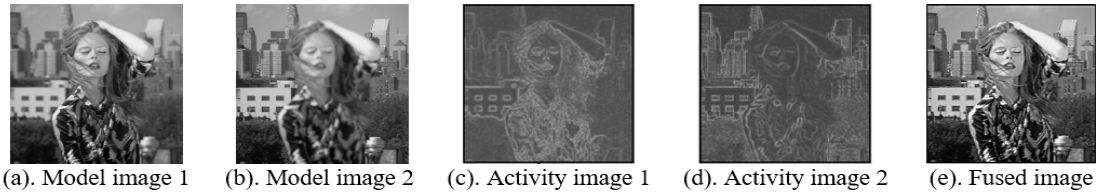

(a). Model image 1 (b). Model image 2 (c). Activity image 1 (d). Activity image 2 (e). Fused image

$W_{3\times3}$ = [0.11, 0.39, 0.50] $W_{5\times5}$ = [0.34, 0.49, 0.17] $W_{7\times7}$ = [0.16, 0.56, 0.28]

FIGURE 4.15: Experimental Results using Model Image with Optimal Weights.

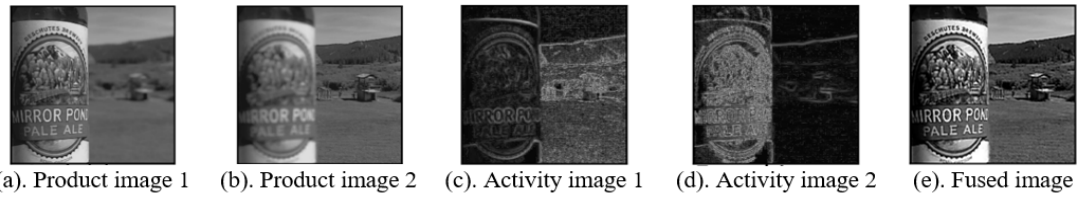

(a). Product image 1 (b). Product image 2 (c). Activity image 1 (d). Activity image 2 (e). Fused image

$W_{3\times3}$ = [0.44, 0.38, 0.18] $W_{5\times5}$ = [0.17, 0.36, 0.47] $W_{7\times7}$ = [0.12, 0.59, 0.29]

FIGURE 4.16: Experimental Results using Product Image with Optimal Weights.

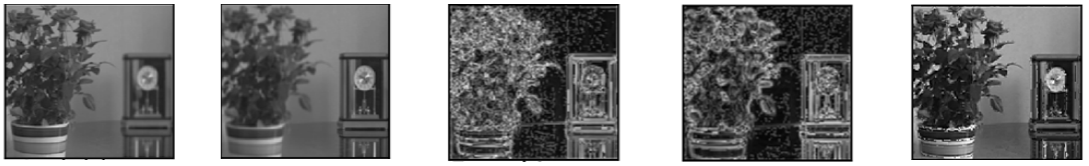

(a). Plant image 1 (b). Plant image 2 (c). Activity image 1 (d). Activity image 2 (e). Fused image

$W_{3\times3}$ = [0.72, 0.16, 0.12] $W_{5\times5}$ = [0.35, 0.36, 0.29] $W_{7\times7}$ = [0.50, 0.17, 0.33]

FIGURE 4.17: Experimental Results using Plant Image with Optimal Weights.

(a). Clock image 1 (b). Clock image 2 (c). Activity image 1 (d). Activity image 2 (e). Fused image

$W_{3\times3}$ = [0.37, 0.33, 0.30] $W_{5\times5}$ = [0.57, 0.30, 0.13] $W_{7\times7}$ = [0.47, 0.31, 0.22]

FIGURE 4.18: Experimental Results using Clock Image with Optimal Weights.

(a). Lab image 1 (b). Lab image 2 (c). Activity image 1 (d). Activity image 2 (e). Fused image

$W_{3\times3}$ = [0.35, 0.49, 0.16] $W_{5\times5}$ = [0.39, 0.14, 0.47] $W_{7\times7}$ = [0.54, 0.35, 0.11]

FIGURE 4.19: Experimental Results using Lab Image with Optimal Weights.

4.3.4.2 Comparison with weighted approaches

The goal of image fusion is to accurately preserve each detail of input images in a fused image. Therefore, fused images are evaluated using certain statistical and mathematical model based quality measures such as NMI, AG and YC respectively. Furthermore, a comparison is performed with previously state-of-the-art fusion methods to find out accuracy of a proposed approach. Figure 4.20, presents a comparison of proposed fusion methodology with previous methodologies such as DCHWT, WSSM, CBF, ICA, CSR have produced lowest evaluation results. Other fusion methodologies such as SRCF and IFM have produced lower evaluation scores than proposed methodology. In this phase, a fused image is created from local features using a patch size of 3×3.

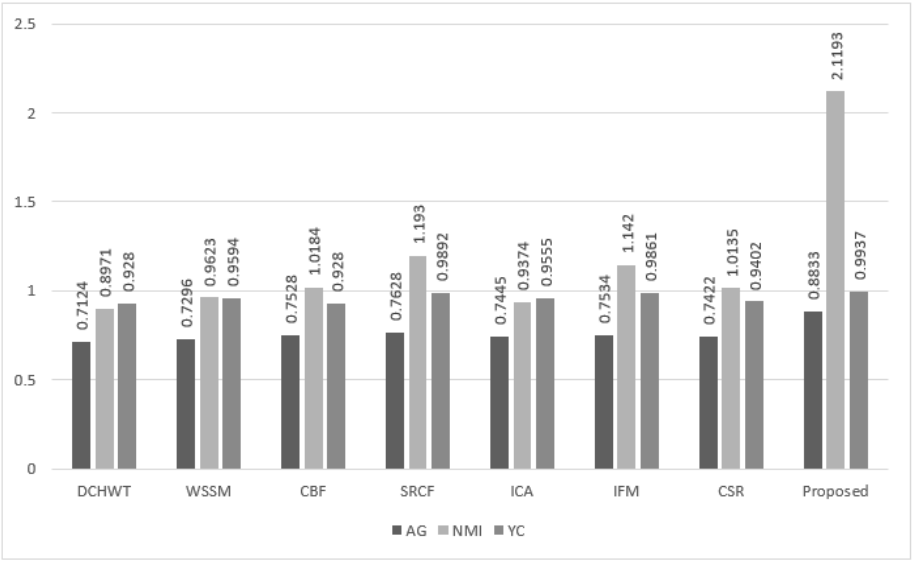

FIGURE 4.20: Comparison of Implemented Approach using Sliding Window of 3×3 with Weighted Approaches.

In Figure 4.21 evaluation results of this experimentation are presented using a comparison with previous weighted fusion methodologies. This experimentation is performed using a local patch size of 5×5. There is a strong evidence that fusion methodologies such as SRCF and IFM have generated promising evaluation scores than this experimentation. However, other approaches such as DCHWT, WSSM, CBF, ICA, CSR have reported lowest evaluation results.

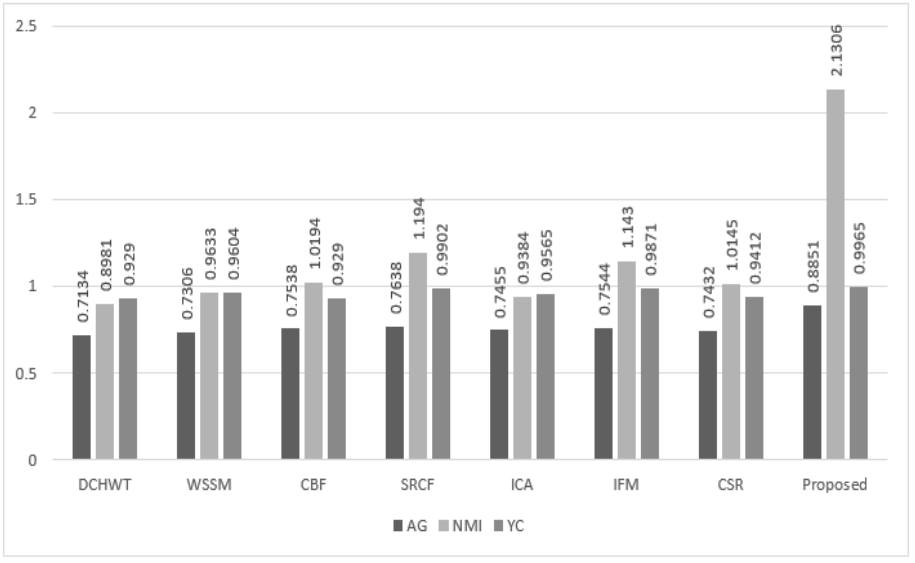

FIGURE 4.21: Comparison of Implemented Approach using Sliding Window of 5×5 with Weighted Approaches.

The evaluation results of this experimentation over a local patch size of 7×7 are presented using a comparison with previous weighted fusion methodologies in figure 4.22. It has been observed from experimental evaluation that fusion methodologies such as DCHWT, WSSM, CBF, ICA, CSR have stated lowest evaluation results. Other weighted methodologies such as SRCF and IFM have generated promising evaluation scores than this experimentation.

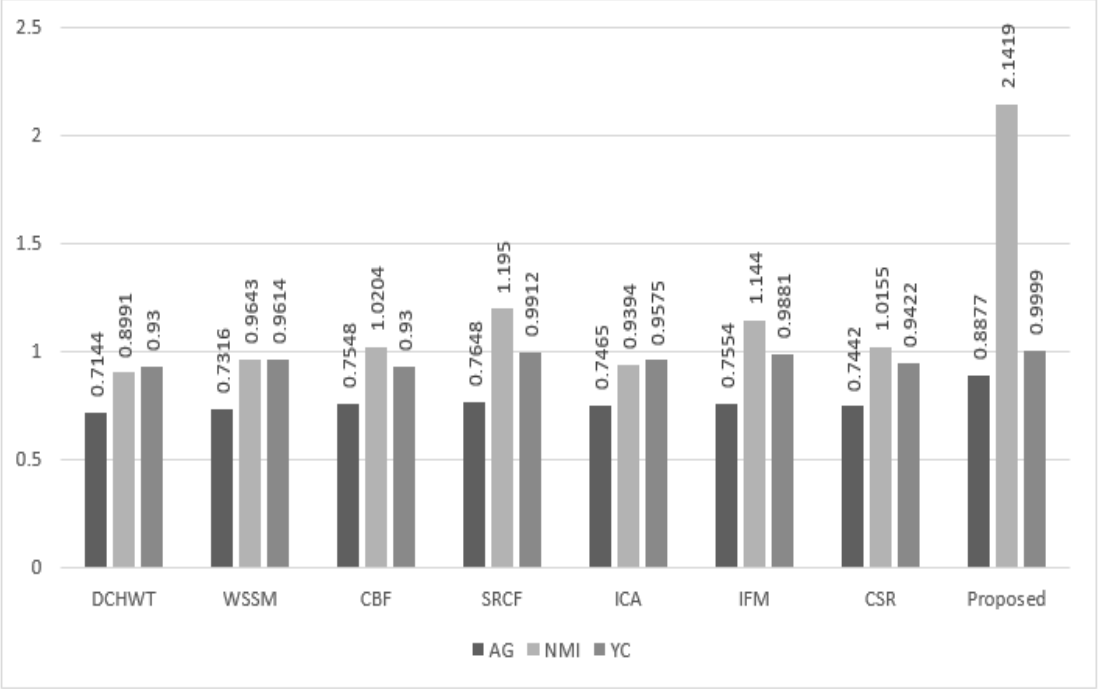

FIGURE 4.22: Comparison of Implemented Approach using Sliding Window of 7×7 with Weighted Approaches.

4.3.4.3 Comparison using non-weighted approaches

Figure 4.23, presents a comparison of proposed fusion methodology with previous non- weighted fusion methodologies. The fusion approaches such as DCTLP, MSTSR, PCA have produced lowest evaluation results. Other fusion methodologies such as PCNN, GIF, DCTV, IFGD, MWGF and CAB have produced closer but lower evaluation scores than proposed methodology. In this phase, a fused image is obtained from local features using a patch size of 3×3. Similarly, the evaluation is also performed over fused images which are created using patches of 5×5 and 7×7 separately.

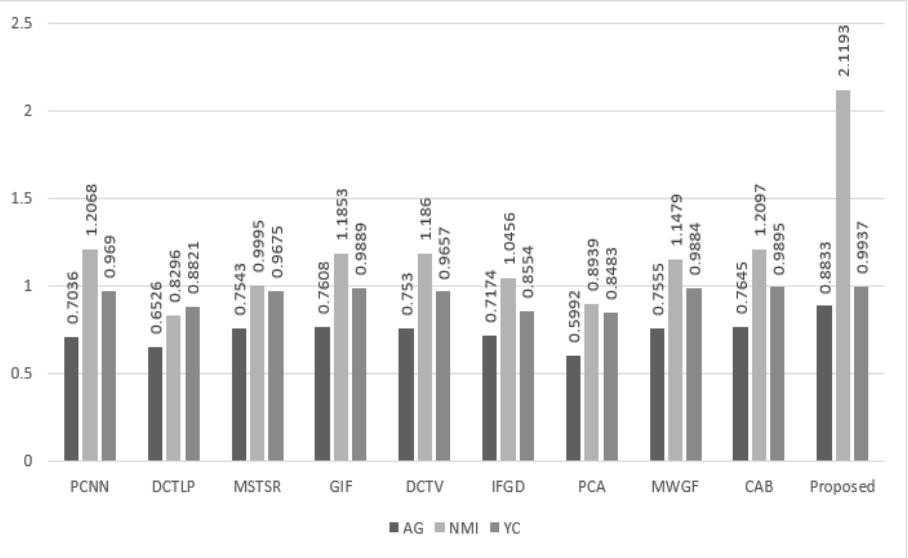

FIGURE 4.23: Comparison of Implemented Approach using Sliding Window of 3×3 with Non-Weighted Approaches.

In Figure 4.24 evaluation results of this experimentation are illustrated using a comparison with previous non-weighted fusion methodologies. In this experimentation, a local patch size of 5×5 is used. It has been observed that fusion methodologies such as PCNN, GIF, DCTV, IFGD, MWGF and CAB have generated proximate but lower evaluation scores than this experimentation. However, other approaches such as DCTLP, MSTSR, PCA have formed lowest evaluation results.

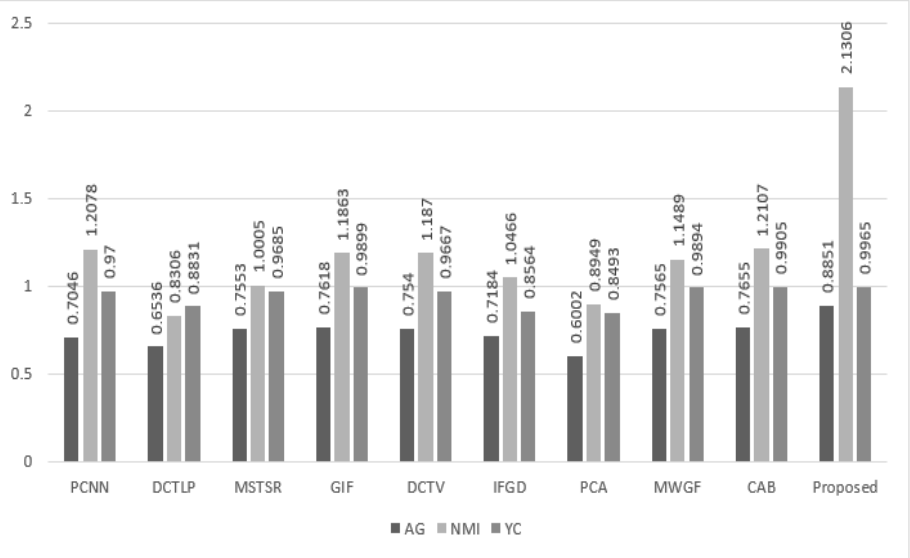

FIGURE 4.24: Comparison of Implemented Approach using Sliding Window of 5×5 with Non-Weighted Approaches.

Figure 4.25 draws a chart of evaluation results of this experimentation over a local patch size of 7×7. In this chart, a comparison of previous non-weighted fusion methodologies with this experimentation is demonstrated. It is evident from this chart that methodologies of DCTLP, MSTSR, PCA have fashioned lowest evaluation results. Fusion methodologies such as PCNN, GIF, DCTV, IFGD, MWGF and CAB have provided proximate but lower evaluation scores than this experimentation.

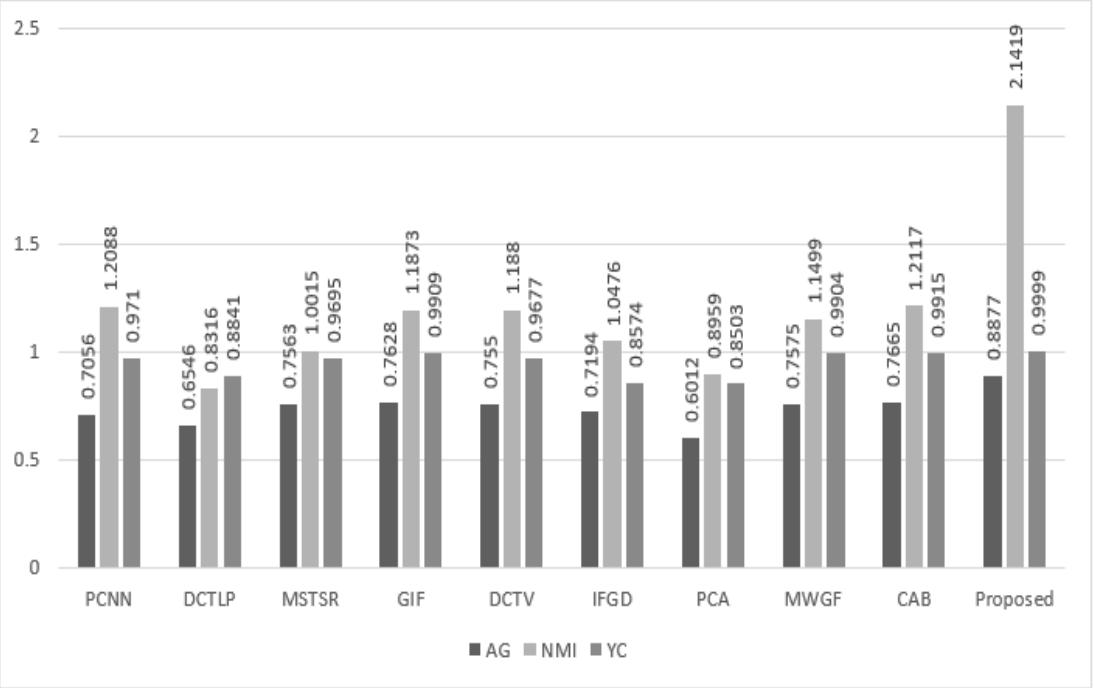

FIGURE 4.25: Comparison of Implemented Approach using Sliding Window of 7×7 with Non-Weighted Approaches.

Chapter 5

Conclusion and Future Work

The domain of image fusion is growing expeditiously and getting more and more attention of the researchers day by day. Image fusion is a process which combines two or more input images to create an all in focused fused image. Earlier studies have addressed this issue with promising results in creating an all in focused complimentary fused image. Furthermore, they have employed different features to characterize focused and non-focused regions in input images. For reconstruction of all in focused fused image, an ensemble of shape and texture based features such as ω_{SO}, ω_{LO} *and* ω_{LBP} is employed. To decide contribution of each feature, the optimal weights are obtained using a Genetic Algorithm. The experimental results have indicated improvement over previously proposed fusion methods.

5.1 Limitations and Future Work

In this dissertation, we have used nine datasets of multi-focus images, where each dataset is a pair of two images. Currently, these are the standard datasets which are publicly available from previous state of the art fusion methods. These datasets consist on eighteen multi-focus images. Although it is a small amount of data, which can only generate a generic conclusion. As this domain lacks a large dataset

of multi-focus image dataset. One direction from this research is the creation of a novel dataset of multi-focus images.

To perform this research an ensemble of three features such as two shape based and one texture based feature is employed. For better characterization of focused and non-focused regions, this ensemble can be increased to n features. Moreover, the optimal weights are obtained from a limited population of five chromosomes because of a higher computational cost. However, this population can also be increased up to n number of chromosomes.

5.2 Research Implications

This research can also be implemented in following areas:

- Medical Imaging.
  - Detection of novel severe acute respiratory syndrome.
  - Detection of neurodegenerative signs.
  - Detection of ductal/prostrate carcinoma.
  - Detection of epidermal parasitic infection
- Agricultural Imaging.
  - Detecting feces over fruits.
  - Identification of fruits/plants quality.

Bibliography

[1] J. Wang, Y. Shen, and S. Yang, "A practical marker-less image registration method for augmented reality oral and maxillofacial surgery," *International journal of computer assisted radiology and surgery*, vol. 14, no. 5, pp. 763–773, 2019.

[2] A. Wibisono, J. Adibah, F. S. Priatmadji, N. Z. Viderisa, A. Husna, and P. Mursanto, "Segmentation-based knowledge extraction from chest x-ray images," in *2019 4th Asia-Pacific Conference on Intelligent Robot Systems (ACIRS)*. IEEE, 2019, pp. 225–230.

[3] M. C. H. Lee, K. Petersen, N. Pawlowski, B. Glocker, and M. Schaap, "Tetris: template transformer networks for image segmentation with shape priors," *IEEE transactions on medical imaging*, vol. 38, no. 11, pp. 2596–2606, 2019.

[4] H. Zhao, Z. Shang, Y. Y. Tang, and B. Fang, "Multi-focus image fusion based on the neighbor distance," *Pattern Recognition*, vol. 46, no. 3, pp. 1002–1011, 2013.

[5] F. Knolle, R. P. Goncalves, and A. J. Morton, "Sheep recognize familiar and unfamiliar human faces from two-dimensional images," *Royal Society Open Science*, vol. 4, no. 11, p. 171228, 2017.

[6] D. J. Ho, C. Fu, P. Salama, K. W. Dunn, and E. J. Delp, "Nuclei detection and segmentation of fluorescence microscopy images using three dimensional convolutional neural networks," in *2018 IEEE 15th International Symposium on Biomedical Imaging (ISBI 2018)*. IEEE, 2018, pp. 418–422.

[7] C. Pohl and J. L. Van Genderen, "Review article multisensor image fusion in remote sensing: concepts, methods and applications," *International journal of remote sensing*, vol. 19, no. 5, pp. 823–854, 2001.

[8] K. Sims, "Artificial evolution for computer graphics," in *Proceedings of the 18th annual conference on Computer graphics and interactive techniques*, 2003, pp. 319–328.

[9] C. Szegedy, V. Vanhoucke, S. Ioffe, J. Shlens, and Z. Wojna, "Rethinking the inception architecture for computer vision," in *Proceedings of the IEEE conference on computer vision and pattern recognition*, 2016, pp. 2818–2826.

[10] N. Alajlan, M. S. Kamel, and G. H. Freeman, "Geometry-based image retrieval in binary image databases," *IEEE transactions on pattern analysis and machine intelligence*, vol. 30, no. 6, pp. 1003–1013, 2008.

[11] B. Goyal, A. Dogra, S. Agrawal, and B. Sohi, "A three stage integrated denoising approach for grey scale images," *Journal of Ambient Intelligence and Humanized Computing*, pp. 1–16, 2018.

[12] A. M. Chaudhry, M. M. Riaz, and A. Ghafoor, "A framework for outdoor rgb image enhancement and dehazing," *IEEE Geoscience and Remote Sensing Letters*, vol. 15, no. 6, pp. 932–936, 2018.

[13] J.-I. Park, M.-H. Lee, M. D. Grossberg, and S. K. Nayar, "Multispectral imaging using multiplexed illumination," in *2007 IEEE 11th International Conference on Computer Vision*. IEEE, 2007, pp. 1–8.

[14] S. Li, J.-Y. Kwok, I.-H. Tsang, and Y. Wang, "Fusing images with different focuses using support vector machines," *IEEE Transactions on neural networks*, vol. 15, no. 6, pp. 1555–1561, 2004.

[15] C. Pohl and J. L. Van Genderen, "Review article multisensor image fusion in remote sensing: concepts, methods and applications," *International journal of remote sensing*, vol. 19, no. 5, pp. 823–854, 2008.

[16] P. Balasubramaniam and V. Ananthi, "Image fusion using intuitionistic fuzzy sets," *Information Fusion*, vol. 20, pp. 21–30, 2014.

[17] V. Aslantas and R. Kurban, "Fusion of multi-focus images using differential evolution algorithm," *Expert Systems with Applications*, vol. 37, no. 12, pp. 8861–8870, 2010.

[18] M. S. Farid, A. Mahmood, and S. A. Al-Maadeed, "Multi-focus image fusion using content adaptive blurring," *Information fusion*, vol. 45, pp. 96–112, 2019.

[19] A. M. Bruckstein, D. L. Donoho, and M. Elad, "From sparse solutions of systems of equations to sparse modeling of signals and images," *SIAM review*, vol. 51, no. 1, pp. 34–81, 2009.

[20] D. E. Newland, "Time-frequency and time-scale signal analysis by harmonic," *Signal Analysis and Prediction*, p. 1, 2005.

[21] J. Zhao, Q. Zhou, Y. Chen, H. Feng, Z. Xu, and Q. Li, "Fusion of visible and infrared images using saliency analysis and detail preserving based image decomposition," *Infrared physics & technology*, vol. 56, pp. 93–99, 2013.

[22] V. Bhavana and H. Krishnappa, "Multi-modality medical image fusion using discrete wavelet transform," *Procedia Computer Science*, vol. 70, pp. 625–631, 2015.

[23] M. S. Kim, A. M. Lefcourt, Y.-R. Chen, and Y. Tao, "Automated detection of fecal contamination of apples based on multispectral fluorescence image fusion," *Journal of food engineering*, vol. 71, no. 1, pp. 85–91, 2005.

[24] K. Ma, K. Zeng, and Z. Wang, "Perceptual quality assessment for multi-exposure image fusion," *IEEE Transactions on Image Processing*, vol. 24, no. 11, pp. 3345–3356, 2015.

[25] B. S. Kumar, "Image fusion based on pixel significance using cross bilateral filter," *Signal, image and video processing*, vol. 9, no. 5, pp. 1193–1204, 2015.

[26] K. Zhan, J. Teng, Q. Li, J. Shi *et al.*, "A novel explicit multi-focus image fusion method," *Journal of Information Hiding and Multimedia Signal Processing*, vol. 6, no. 3, pp. 600–612, 2015.

[27] V. Naidu and J. R. Raol, "Pixel-level image fusion using wavelets and principal component analysis," *Defence Science Journal*, vol. 58, no. 3, p. 338, 2008.

[28] X. Qu, C. Hu, and J. Yan, "Image fusion algorithm based on orientation information motivated pulse coupled neural networks," in *2008 7th World Congress on Intelligent Control and Automation.* IEEE, 2008, pp. 2437–2441.

[29] M. Nejati, S. Samavi, and S. Shirani, "Multi-focus image fusion using dictionary-based sparse representation," *Information Fusion*, vol. 25, pp. 72–84, 2015.

[30] Z. Zhou, S. Li, and B. Wang, "Multi-scale weighted gradient-based fusion for multi-focus images," *Information Fusion*, vol. 20, pp. 60–72, 2014.

[31] C. Hsieh and W. Wu, "Pixel-based multi-focus image fusion by color appearance model," in *Software Engineering and Information Technology: Proceedings of the 2015 International Conference on Software Engineering and Information Technology (SEIT2015).* World Scientific, 2016, pp. 255–260.

[32] Y. Liu, S. Liu, and Z. Wang, "Multi-focus image fusion with dense sift," *Information Fusion*, vol. 23, pp. 139–155, 2015.

[33] H. Yin, Y. Li, Y. Chai, Z. Liu, and Z. Zhu, "A novel sparse-representation-based multi-focus image fusion approach," *Neurocomputing*, vol. 216, pp. 216–229, 2016.

[34] B. Zhang, X. Lu, H. Pei, H. Liu, Y. Zhao, and W. Zhou, "Multi-focus image fusion algorithm based on focused region extraction," *Neurocomputing*, vol. 174, pp. 733–748, 2016.

[35] H. Tang, B. Xiao, W. Li, and G. Wang, "Pixel convolutional neural network for multi-focus image fusion," *Information Sciences*, vol. 433, pp. 125–141, 2018.

[36] W. Chantara and Y.-S. Ho, "Multi-focus image fusion for extended depth of field," in *Proceedings of the 10th International Conference on Internet Multimedia Computing and Service*, 2018, pp. 1–4.

[37] C. Wang, R. Yuan, Y. Sun, Y. Jiang, C. Chen, and X. Lin, "A new method of multi-focus image fusion using laplacian operator and region optimization," *Journal of Computer and Communications*, vol. 6, no. 5, pp. 106–118, 2018.

[38] S. Li, X. Kang, J. Hu, and B. Yang, "Image matting for fusion of multi-focus images in dynamic scenes," *Information Fusion*, vol. 14, no. 2, pp. 147–162, 2013.

[39] S. Paul, I. S. Sevcenco, and P. Agathoklis, "Multi-exposure and multi-focus image fusion in gradient domain," *Journal of Circuits, Systems and Computers*, vol. 25, no. 10, p. 1650123, 2016.

[40] Y. Liu, X. Chen, R. K. Ward, and Z. J. Wang, "Image fusion with convolutional sparse representation," *IEEE signal processing letters*, vol. 23, no. 12, pp. 1882–1886, 2016.

[41] M. Nikolaos and N. Tania, "Pixel-based and region-based image fusion schemes using ica bases," *Information Fusion*, vol. 8, no. 2, pp. 131–142, 2007.

[42] K. B. K. Shreyamsha, "Multifocus and multispectral image fusion based on pixel significance using discrete cosine harmonic wavelet transform," *Signal, Image and Video Processing*, vol. 7, no. 6, pp. 1125–1143, 2012.

[43] N. VPS and E. Bindu, "A novel image fusion technique using dct based laplacian pyramid," *International Journal of Inventive Engineering and Sciences (IJIES)*, vol. 1, no. 2, pp. 1–9, 2013.

[44] Mohammad, Bagher, Akbari, A. Haghighat, H. Aghagolzadeh, and Seyedarabi, "Multi-focus image fusion for visual sensor networks in dct domain," *Computers and Electrical Engineering*, vol. 37, no. 5, pp. 789–797, 2011.

[45] Jing, L. Tian, and Chen, "Adaptive multi-focus image fusion using a wavelet-based statistical sharpness measure," *Signal Processing*, vol. 92, no. 9, pp. 2137–2146, 2012.

[46] Yu, S. Liu, Z. Liu, and Wang, "A general framework for image fusion based on multi-scale transform and sparse representation," *Information Fusion*, vol. 24, no. 1, pp. 147–164, 2014.

[47] Kumar, Prema, R. P. M, and Kumar, "Enhancing bio-medical mammography image fusion using optimized genetic algorithm," *Journal of Medical Imaging and Health Informatics*, vol. 9, no. 3, pp. 1–6, 2019.

[48] J. S., R. S. Kulkarni, and Bichkar, "Optimization in image fusion using genetic algorithm," *International Journal of Image, Graphics and Signal Processing*, vol. 8, no. 1, pp. 50–59, 2019.

[49] Gehad, Mohamed, M. Taher, Elsayed, G. Wahed, El, A. Taweal, and Fouad, "Image fusion approach with noise reduction using genetic algorithm," *International Journal of Advanced Computer Science and Applications*, vol. 4, no. 11, pp. 10–16, 2013.

[50] Anil, A. Kumbhar, U. Kulkarni, and Sutar, "Fusion of multiple features in magnetic resonant image segmentation using genetic algorithm," in *3rd IEEE International Advance Computing Conference (IACC)*. IEEE, 2013, pp. 819–825.

[51] Richa, D. Gupta, and Awasthi, "Wave-packet image fusion technique based on genetic algorithm," in *5th International Conference-Confluence The Next Generation Information Technology Summit (Confluence)*. IEEE, 2014, pp. 280–285.

[52] T. Ojala, M. Pietikäinen, and D. Harwood, "A comparative study of texture measures with classification based on featured distributions," *Pattern recognition*, vol. 29, no. 1, pp. 51–59, 2006.

[53] Z. Jin-Yu, C. Yan, and H. Xian-Xiang, "Edge detection of images based on improved sobel operator and genetic algorithms," in *2009 International Conference on Image Analysis and Signal Processing*. IEEE, 2009, pp. 31–35.

[54] D. Marr and E. Hildreth, "Theory of edge detection," *Proceedings of the Royal Society of London. Series B. Biological Sciences*, vol. 207, no. 1167, pp. 187–217, 2011.

[55] X. Yi and M. Eramian, "Lbp-based segmentation of defocus blur," *IEEE transactions on image processing*, vol. 25, no. 4, pp. 1626–1638, 2016.

[56] O. Kramer, *Genetic algorithm essentials*. Springer, 2017, vol. 679.

[57] M. Hossny, S. Nahavandi, and D. Creighton, "Comments on'information measure for performance of image fusion'," *Electronics letters*, vol. 44, no. 18, pp. 1066–1067, 2008.

[58] C. Xydeas, , and V. Petrovic, "Objective image fusion performance measure," *Electronics letters*, vol. 36, no. 4, pp. 308–309, 2000.

[59] S. Li, R. Hong, and X. Wu, "A novel similarity based quality metric for image fusion," in *2008 International Conference on Audio, Language and Image Processing*. IEEE, 2008, pp. 167–172.